Copernicus assisted environmental monitoring across the Black Sea Basin – PONTOS

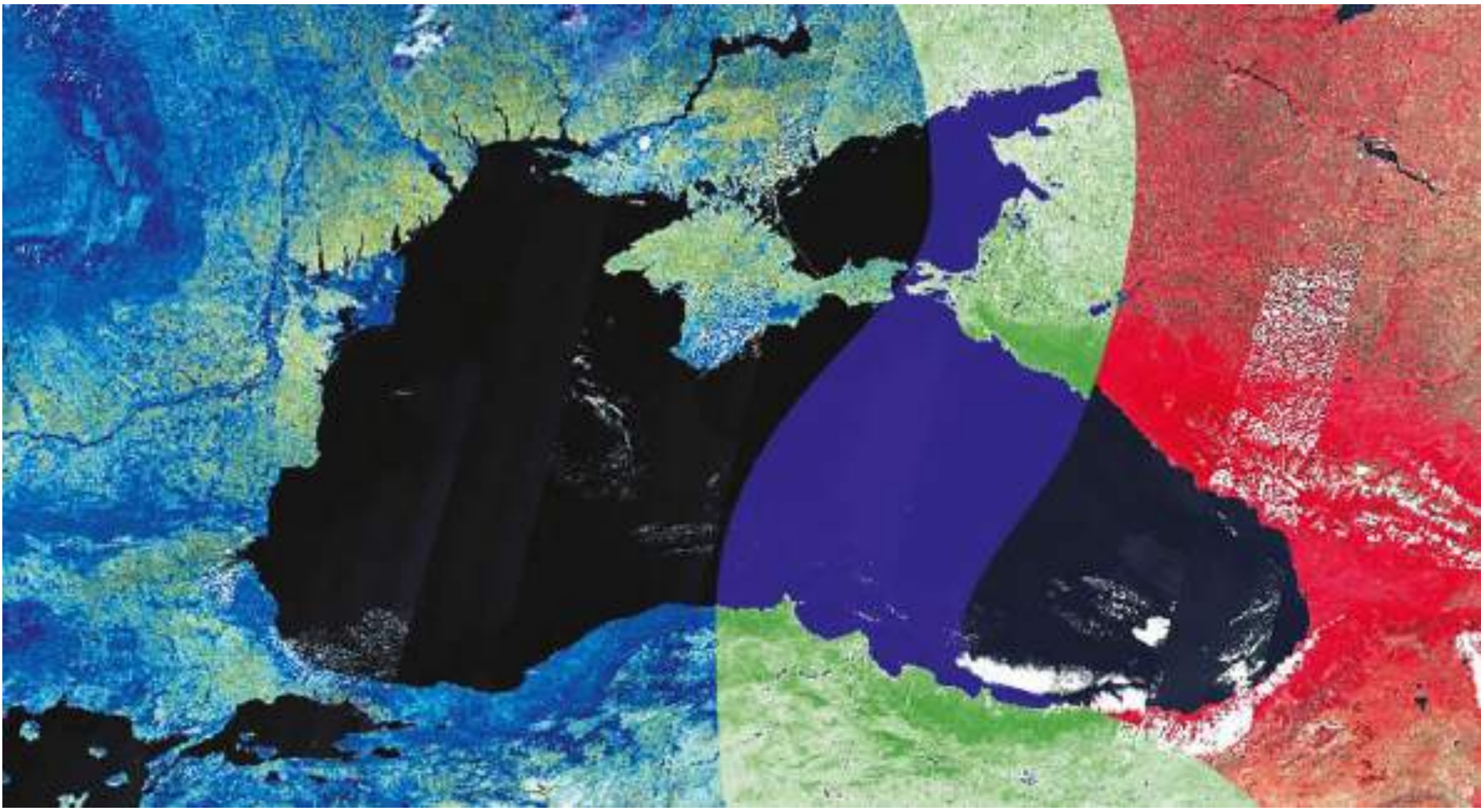

Integrated assessment on chlorophyll concentration and eutrophication dynamics

Deliverable D.T1.2.5

PONTOS-GR (Greece)

Table of Contents

1 Introduction

Coastal lagoons are considered unique, complex ecosystems with significant environmental and socioeconomic value (Jimeno-Sáez et al., 2020; Sylaios and Theocharis, 2002). They form shallow coastal water bodies, mostly situated in river deltaic zones, being isolated from the sea by a sand barrier, land spit or other similar geomorphic feature, originating from the sediment outflux of the adjacent river. Lagoons are connected to the sea by one or more tidal inlets, through which the lagoon basin communicates with the open sea (Kjerfve, 1994). The geometric characteristics of these inlets (length, width, depth) govern the exchange dynamics and fluxes of water, salt, nutrient and SPM between the lagoon's basin and the open sea, classifying them into flood- or ebb-dominated systems. In flood-dominated systems, flood prevails over ebb within a typical tidal cycle, meaning that influx is stronger than outflux. These are relatively deep entrance inlets with high inlet cross-sectional (A_C) to lagoon basin (A_b) areas ratio. On the contrary, in ebb-dominated lagoons, ebb prevails over flood, meaning that outflux is stronger than influx. The distortion of the tidal signal through the inlet necessarily impacts the water flow between the ocean and the lagoon, and a strong asymmetry of the current velocity occurs, known as residual circulation capable to carry pollutants and sediments.

Lagoons are considered of high ecological value, as recognized by European legislation through the application of the Habitats Directive and the Natura 2000 network, providing a series of ecosystem services, including fish production, biodiversity conservation, nutrient cycling, pollutants removal such as heavy metals (Costanza et al., 1997; Zanchettin et al., 2007). They act as transitional buffer zones for the transfer of freshwater and substances from the terrestrial to the coastal zones. A portion of the chemical compounds entering the lagoon environment from the land or the sea is deposited into the lagoonal sediments, making the systems extremely delicate to retain their ecological balance. Environmental degradation caused by alterations in watershed hydrology, pollution and human activities affects the capacity of the lagoon to deliver the above ecosystem services (Kjerfve, 1994).

The great variety of anthropogenic pressures alters the balance of the coastal lagoon ecosystem, making crucial the need for consistent monitoring and management of these territories. One of the major threats these systems face is eutrophication, defined as the accelerated primary production and the occurrence of increased biomass of primary producers, such as phytoplankton, due to nutrient over-enrichment (Devlin et al., 2011). Eutrophication problems associated with human activities have been identified as one of the main causes of water quality deterioration of coastal ecosystems (Kadiri et al., 2021). Several negative impacts are associated with eutrophication: the accelerated phytoplankton production limits sunlight availability to benthic aquatic plants; depletes dissolved oxygen in the water column, and especially at the bottom, due to decomposition of accumulated biomass resulting in hypoxic or anoxic conditions; and decreases species diversity and abundance.

This could give rise to shifts in invertebrate communities and permanent changes in aquatic habitats, with negative implications for pelagic and benthic fauna, including fish stocks. For example, a high fish mortality rate was reported in Ismarida lake in August 2013

(Koutrakis et al., 2016) and in Vistonida lagoon in July 2014. Eutrophication could also lead to algal toxin production, with a wider range of toxic species reported in estuarine environments, compared to freshwater environments, which could significantly affect the edibility of local seafood (Shumway, 1990). Such adverse effects may trigger negative socio-economic consequences, becoming significant over time.

The phytoplankton biomass, represented by chlorophyll-a (Chl-a), is an important indicator to evaluate the state of eutrophication in water bodies, thus helpful in coastal ecosystem monitoring and management. Systematic monitoring in coastal ecosystems is essential, but in-situ monitoring (e.g., water sample collection and analysis in the laboratory) is a time and money consuming method and is laborious to adequately assess the entire system on a regular basis. Satellite remote sensing is a feasible way to monitor water bodies when water quality over large regions has to be monitored with regular frequency. There is also the possibility to estimate water quality in non-accessible water bodies. However, passive satellite monitoring is heavily dependent upon weather, air mass temperature changes and sunlight conditions, which directly affect the quality and quantity of useful data.

The objective of this study is to map and assess Chl-a concentration in the coastal lagoons of Northern Greece. Those coastal lagoons have cultural, environmental and economic importance, therefor monitoring is needed to address the water quality changes. We focus on the study of the temporal and spatial evolution of Chl-a for the period 2013-2021. Landsat 8 satellite images were retrieved and processed for the time period 2013-2015 and Sentinel-2 images for the period 2015-2021.

Chl-a values were initially assessed using the well-known C2RCC algorithm. This algorithm has been validated in the open sea environment of Case 1 (in which their inherent optical properties are dominated by phytoplankton, e.g., most open ocean waters) and Case 2 waters (containing colored dissolved organic matter (CDOM) and inorganic mineral particles in addition to phytoplankton. However, the interference of (a) the shallow sea bottom reflection, (b) the sun glint and (c) the presence of non-algal particles on the optical signal (spectral reflectances) measured by satellites has not been adequately evaluated. In this report, we attempted to recalibrate the C2RCC processor using in-situ Chl-a concentration data and the respective spectral reflectance values for the appropriate training of a Takagi-Sugeno neuro-fuzzy algorithm to correct the satellite-derived Chl-a values.

Figure 1 explains graphically the steps to be followed for this analysis.

Figure 1. Methodological steps followed in present study.

1.1 Satellite Remote Sensing and Chlorophyll-a Algorithms

The Water Framework Directive (WFD, 2000/60/EC) obligates all European Union (EU) member states to implement water management and estimate the ecological status of water bodies, through systematic monitoring and classification. The measurement of Chl-a in water is commonly used (a) as an indicator to monitor water quality in coastal and inland waters, (b) in the surveillance of harmful algal blooms (HABs), (c) and in ecological studies of phytoplankton biomass and productivity (Jordan et al., 1991; Morrow et al., 2000). Deriving the chlorophyll concentration associated with algal blooms is an important metric which provides quantitative algal biomass measures useful in documenting the severity of blooms and their long-term trends, especially in relation to nutrient targets and water quality guidelines. Moreover, Chl-a has also been used as an indicator of cyanobacteria (Ogashawara and Moreno-Madriñán, 2014). Other water quality indicators like total suspended matter (TSM), turbidity, Secchi depth and colored dissolved organic matter (CDOM) can also be measured using remote sensing techniques (Toming et al., 2016).

Remote sensing has been used for decades to estimate Chl-a concentration, most notably with operational applications in the oceans (Hu et al., 2012; Mobley, 1995; O'Reilly et al., 1998; Schalles, 2006). However, significant progress has been made in applying remote sensing in inland water bodies with positive outcomes, as described in Palmer et al. (2015) and Bukata (2013). The main challenge to use remote sensing is to isolate the Chl-a signal from other cell components and other optically active compounds and the effects of the vertical distribution variation of chlorophyll in the water column.

The first satellite sensor developed to evaluate Chl-a concentration was the Coastal Zone Color Scanner (CZCS) onboard Nimbus 7 which was launched in late 1978. A two-band ratio of 443–550 nm was calibrated and routinely used for Chl-a estimation (O'Reilly et al., 1998). Two more operational sensors were also developed for the monitoring of Chl-a concentration using bands in the blue and the green regions (Sea-viewing Field of view sensor—SeaWIFS-and Moderate resolution Imaging Spectroradiometer — MODIS) (O'Reilly et al., 1998; Schalles, 2006).

The Chl-a algorithms in ocean waters are based on a simple interaction of phytoplankton density with water, in which usually blue to green band ratios have a robust and sensitive relation to Chl-a during low concentration levels (1–30 mg/m^3). This relationship becomes less sensitive at higher Chl-a concentration (above 30 mg/m^3) and is highly compromised by the effects of colored dissolved organic matter (CDOM) in turbid and optically complex waters (Schalles, 2006). Indeed, chlorophyll retrieval algorithms adopting blue to green band ratios have been shown to be robust for offshore waters, but are known to be sensitive to interference from non-algal constituents (particularly CDOM), as well as uncertainties brought about by atmospheric correction failure over highly turbid waters.

The distinct scattering/absorption features of Chl-a are the strong absorption between 400–500 nm (blue) and 680 nm (red), and the reflectance maximums at 550 nm (green) and 700nm (near-infrared-NIR) (Han, 1997). Wavelength range for characterizing Chl-a is between 400 nm and 900 nm (Han and Jordan, 2005). Therefore, the four bands mostly associated with Chl-a are the blue, green, red and NIR bands (Han, 1997; Yew-Hoong Gin et al., 2002).

According to Schalles (2006), low Chl-a concentration (<2 mg/m^3) shows higher reflectance in the blue part of the spectrum (400–500 nm) and reflectance decreases as wavelength increases, with extremely low reflectance values, near 0, in the near infrared spectrum (NIR, 700–800 nm); Chl-a concentrations between 2 and 30 mg/m^3 show higher reflectance in the green (500–600 nm) and red bands (600–700 nm), with peak reflectance in the green part of the spectrum; and Chl-a concentrations over 300 mg/m^3, show peak reflectance in the NIR and minimum high in the green part of the spectrum, the blue and red bands show low reflectance.

These principles are used to select bands and develop algorithms to retrieve Chl-a from satellite images since it is evident that spectral signature changes depending on the content of Chl-a in water. Usually, local-based algorithms are needed for inland water bodies, and they vary significantly from one site to another since their development is based on the specific optical constituents of a water body.

These operational algorithms are based on comparing blue to green ratios and have been generated for oceanic waters in which color is dominated by phytoplankton. The largest value of the ratios is used in a fourth-order polynomial regression equation, as the exponential term in a power function equation. These exponential equations best represent the sigmoidal relationship between Chl-a and the band ratio calculations (O'Reilly et al., 1998). The good performance of blue and green ratios in oceanic waters is due to the general tendency that as the phytoplankton concentration increases, reflectance decreases in the blue (400–515 nm) and increases in the green (515–600 nm) (Kirk, 1994). Ocean color and meteorological instruments have a coarse spatial resolution which precludes their applications to small inland lakes (Cao et al., 2020).

Some efforts have been made to find suitable sensors, but none were specifically designed for inland waters. Many lake Chl-a estimations were performed using ocean satellites color sensors including the Coastal Zone Color Scanner (Antoine et al., 1996), SeaWiFS (Dall'Olmo et al., 2005) and Earth Observation Systems, e.g., Moderate Resolution Imaging Spectroradiometer (Gitelson et al., 2008), Medium Resolution Imaging Spectrometer (MERIS) (Gitelson et al., 2008; Gurlin et al., 2011), meteorological satellite, like Advanced Very High Resolution Radiometer (Ibelings et al., 2003), and medium to high resolution land resources satellite, such as Landsat Operational Land Imager (OLI) (Liu et al., 2020) and Sentinel Multispectral Imager (MSI) (Toming et al., 2016).

The launch of Multispectral Imager's (MSI) onboard Copernicus Sentinel-2 mission in 2015 opened a great new potential in small water bodies remote sensing. The derived imagery comes with a spatial resolution of 10 m, 20 m and 60 m, depending on the band, exposing the monitoring of small waterbodies with more sophisticated algorithms based on neural networks, like the Case-2 Regional CoastColour (C2RCC) developed by ESA CoastColour project.

The Sentinel 3A satellite sensor OLCI (Ocean and Land Colour Instrument) launched in February 2016 by the European Space Agency (ESA) is particularly useful for chlorophyll retrievals due to their waveband selection in the red and near-infra-red (R-NIR) portion of the spectrum.

Algorithm approaches exploiting the R-NIR perform well in turbid eutrophic waters and line-height algorithms, such as the Maximum Chlorophyll Index (MCI), the Cyanobacteria Index (CI) and the Maximum Peak Height (MPH), are particularly favorable due to their relative insensitivity to uncertainties in atmospheric correction. Indeed, the application of line-height algorithms to uncorrected or partially atmospherically-corrected (using the bottom of Rayleigh reflectance) aquatic colored satellite data has become increasingly popular. The MCI, CI and MPH indices are well validated for the detection of dense surface algal blooms and have been calibrated for quantitative mapping of chlorophyll concentrations in a range of coastal and inland waters. Similarly, phycocyanin (PC) is a frequently used cyanobacteria marker pigment and forms the basis of many proposed remote sensing algorithms for detecting cyanobacteria.

2 Materials and Methods

2.1 In situ data collection

Field measurements were carried out during the period 2015-2018, from the shallow parts of the lagoons under study. Water samples from the surface of the lagoons were collected and Chl-a concentration was determined. A database of 130 Chl-a values is created. Those in-situ Chl-a concentration values were used to evaluate and calibrate the remote sensing algorithms using the Takagi-Sugeno neurofuzzy model.

2.2 Remote sensing images

2.2.1 Copernicus Sentinel-2 Mission

The Copernicus Sentinel-2 mission comprises a constellation of two polar-orbiting satellites placed in the same sun-synchronous orbit, phased at 180° to each other. It aims at monitoring the variability in land surface conditions, and its wide swath width (290 km) and high revisit time (10 days at the equator with one satellite, and 5 days with 2 satellites under cloud-free conditions, which results in 2-3 days at mid-latitudes) will support monitoring of Earth's surface changes. Sentinel-2 satellites are on track from 2015 to today and image data files consist of twelve spectral bands with a maximum resolution of 10 m (Table 1).

Table 1. Spectral bands, central wavelengths (nm) and corresponding spatial resolutions (m) of Sentinel-2 MSI sensor.

Bands		Central wavelength (nm)	Spatial Resolution (m)
Band 1	**Coastal aerosol**	443	60
Band 2	**Blue**	490	10
Band 3	**Green**	560	10
Band 4	**Red**	665	10
Band 5	**Red Edge-1**	705	20
Band 6	**Red Edge-2**	740	20
Band 7	**Red Edge-3**	783	20
Band 8	**NIR**	842	10
Band 8A	**NIR Vapor**	865	20
Band 9	**Water Vapor**	945	60
Band 10	**SWIR-Cirrus**	1375	60
Band 11	**SWIR-1**	1.610	20
Band 12	**SWIR-2**	2190	20

2.2.1.1 Sentinel- 2 Data

Sentinel-2 (2A and 2B) imagery was retrieved from Sentinel Scientific Data Hub (https://scihub.copernicus.eu/) and Earth Explorer (https://earthexplorer.usgs.gov/) databases. Sentinel-2 products are a compilation of elementary granules of fixed size, along with a single orbit. A granule is the minimum indivisible partition of a product (containing all possible spectral bands). For Level-1C and Level-2A (Figure 2), the granules, also called tiles, are 100 × 100 km ortho-images in UTM/WGS84 projection that divides the Earth's surface into 60 zones. Each UTM zone has a vertical width of 6° of longitude and horizontal width of 8° of latitude.

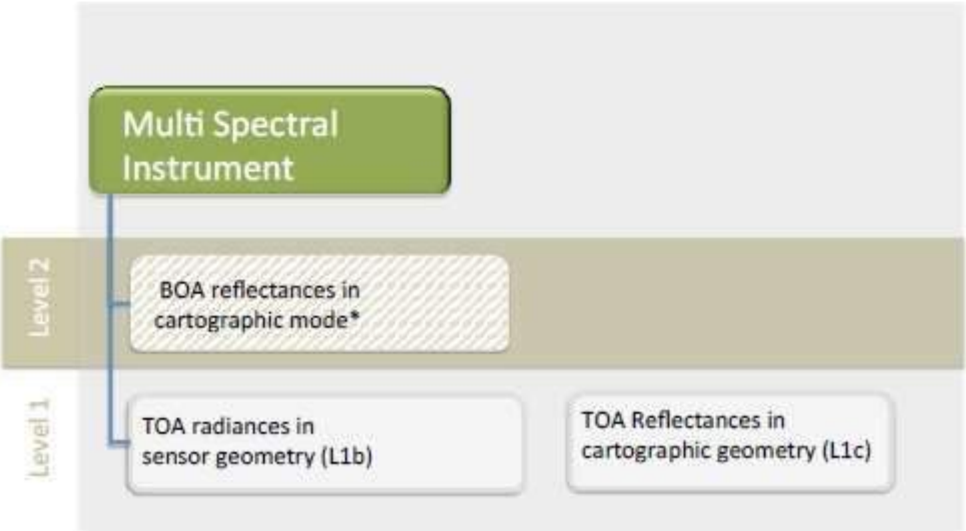

Figure 2. Graphical Representation of Sentinel-2 Core Products.

In this study the historical satellite images were retrieved for the tiles T34TGL, T35TKF and T35TLF in order to cover the entire area of the Greek Pilot area and the period from the early 2015 to 2021 (Figure 3).

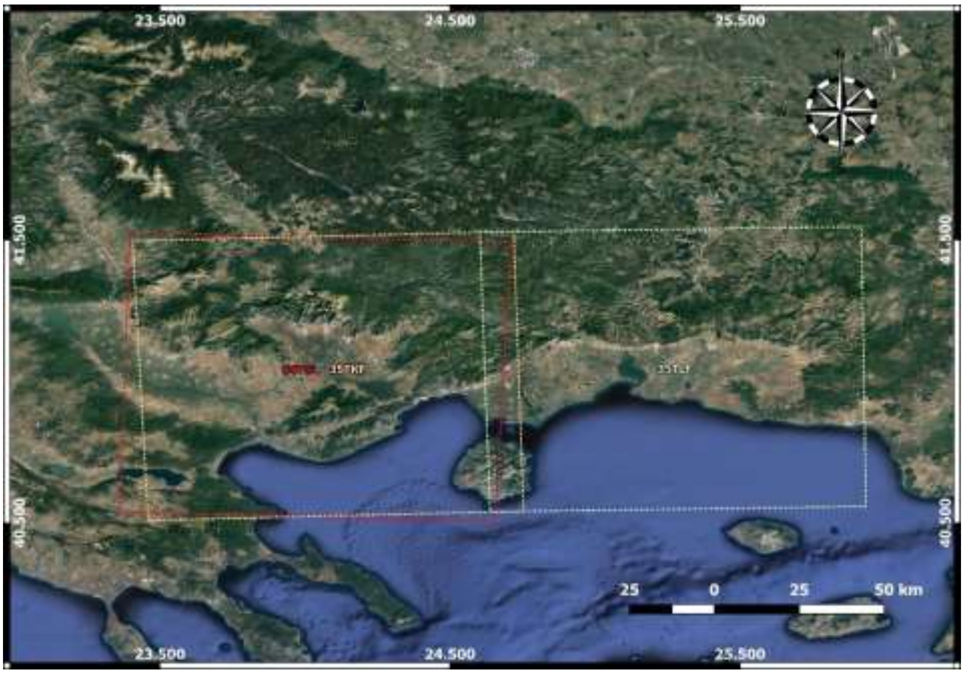

Figure 3. Sentinel-2 tiles over study area of Greek Pilot site (Nestos delta zone).

The satellite images with clouds over the study sites were not used for the Chl-a determination analysis. All images were retrieved in L1C product in order to use the same atmospheric correction for all of them. The number of retrieved images appear in Table 2.

Table 2. Retrieved images from Sentinel-2 mission for each lagoon through years 2015-2021.

Year	Tile	Vassova	Eratino	Agiasma	Porto Lagos	Xirolimni	Ptelea
2015	**T34TGL**	8	8	8			
	T35TKF	1	1	1			
	T35TLF				8	8	8
2016	**T34TGL**	3	3	3			
	T35TKF	1	1	1			
	T35TLF				6	6	6
2017	**T34TGL**	17	17	17			
	T35TKF	3	3	3			
	T35TLF				22	22	22
2018	**T34TGL**	31	31	31			
	T35TKF	1	1	1			
	T35TLF				31	31	31
2019	**T34TGL**	21	21	21			
	T35TKF	12	12	12			
	T35TLF				28	28	28
2020	**T34TGL**	44	44	44			
	T35TKF	1	1	1			
	T35TLF				47	47	47
2021	**T34TGL**	14	14	14			
	T35TLF				13	13	13
Sum		157	157	157	155	155	155

2.2.2 Landsat 4-5 Thematic Mapper (TM)

The Landsat sensors have been widely used for the estimation of optically-related water quality parameters, such as total Chl-a, suspended matter, turbidity, Secchi disk depth, total phosphorus, dissolved oxygen, chemical oxygen demand (COD), and biochemical oxygen demand (BOD) (Gholizadeh et al., 2016; Ouma et al., 2020). The 30-m spatial resolution of their images allows measurements even on small water systems (~ 0.08 km^2) (Brezonik et al., 2005).

Landsat 4-5 was on board from July 1982 to May 2012. It carries the Landsat Thematic Mapper (TM) sensor and has a 16-day repeat cycle. Their image data files consist of seven spectral bands (Table 3) and the resolution is 30 m for bands 1 to 7 (thermal infrared band 6 was collected at 120 m, but was resampled to 30 meters). The approximate scene size is 170 km north-south by 183 km east-west.

Table 3. Spectral bands, wavelengths (nm) and corresponding spatial resolutions (m) of Landsat 4-5.

Band		Wavelength (µm)	Resolution (m)
B1	**Blue**	0.45-0.52	30
B2	**Green**	0.52-0.60	30
B3	**Red**	0.63-0.69	30
B4	**NIR**	0.76-0.90	30
B5	**SWIR-1**	1.55-1.75	30
B6	**TIR**	10.4-012.50	120 (30)
B7	**SWIR-2**	2.08-2.35	30

2.2.3 Landsat 7 Enhanced Thematic Mapper Plus (ETM+)

Landsat 7 was launched in April 1999 carrying the Enhanced Thematic Mapper Plus (ETM+) sensor. This instrument is an improved version of the Thematic Mapper instruments that were onboard Landsat 4 and Landsat 5. Landsat 7 orbits the Earth at 705 km in a sun-synchronous, near-polar orbit (98.2 degrees inclination) and has a 16-day repeat cycle with an equatorial crossing time: 10:00 a.m.

Landsat 7 images consist of eight spectral bands (Table 4) with a spatial resolution of 30 m for Bands 1 to 7. The resolution for Band 8 (panchromatic) is 15 m. Approximate scene size is 170 km north-south by 183 km east-west.

2.2.4 Landsat 8

The Landsat 8 mission launched in February 2013 and orbits the Earth in a sun-synchronous, near-polar orbit (98.2 degrees inclination) and has a 16-day repeat cycle with an equatorial crossing time of 10:00 a.m. +/- 15 minutes.

Landsat 8 mission carries the Operational Land Imager (OLI) and the Thermal Infrared Sensor (TIRS) instruments. The OLI comprises 9 bands, measuring in the visible, near infrared, and shortwave infrared portions (VNIR, NIR, and SWIR) of the spectrum. The TIRS includes 2 bands and measures land surface temperature in two thermal bands with a new technology that applies quantum physics to detect heat. These two sensors provide seasonal coverage of the global landmass at a spatial resolution of 30 meters (visible, NIR, SWIR); 100 meters (thermal); and 15 meters (panchromatic).

Table 4. Spectral bands, wavelengths (nm) and corresponding spatial resolutions (m) of Landsat 7 and 8.

Landsat 7				**Landsat 8**			
Band		**Wavelength (µm)**	**Spatial Resolution (m)**	**Band**		**Wavelength (µm)**	**Spatial Resolution (m)**
				B1	**Coastal/Aerosol**	0.435-0.451	30
B1	**Blue**	0.441-0.514	30	**B2**	**Blue**	0.452-0.512	30
B2	**Green**	0.519-0.601	30	**B3**	**Green**	0.533-0.590	30
B3	**Red**	0.631-0.692	30	**B4**	**Red**	0.636-0.673	30
B4	**NIR**	0.772-0.898	30	**B5**	**NIR**	0.851-0.879	30
B5	**SWIR-1**	1.547-1.749	30	**B6**	**SWIR-1**	1.566-1.651	30
B7	**SWIR-2**	2.064-2.345	30	**B7**	**SWIR-2**	2.107-2.294	30
B8	**Panchromatic**	0.515-0.896	15	**B8**	**Panchromatic**	0.503-0.676	15
				B9	**Cirrus**	1.363-1.384	30
B6	**TIR**	10.31-12.36	60	**B10**	**TIR-1**	10.60-11.19	100
				B11	**TIR-2**	11.500-12.510	100

The OLI sensor is compatible with the earlier Landsat sensors and presents improved measurement capabilities. It provides two new spectral bands, one tailored especially for detecting cirrus clouds and the other for coastal zone observations. TIRS collects data for two more narrow spectral bands in the thermal region formerly covered by one wide spectral band on Landsats 4–7. The 100 m TIRS data is registered to the OLI data to create radiometrically, geometrically, and terrain-corrected 12-bit data products.

2.2.4.1 Landsat 8 Data

Landsat 8 imagery was retrieved from Earth Explorer database (https://earthexplorer.usgs.gov/). The scene size is approximately 170 km north-south by 183 km east-west.

In this study the historical satellite images with path and row (183,31), (183,32) and (182,32) were retrieved in order to cover the Greek Pilot area for the period 2013-2015.

All images were retrieved in L1C product in order to use the same atmospheric correction for all of them. The number of retrieved images appear in Table 5.

Table 5. Retrieved images from Landsat 8 for each lagoon through years 2015-2021.

Year	Path	Row	Greek Pilot area
2013	**183**	**32**	11
	183	**31**	10
	182	**32**	10
2014	**183**	**32**	7
	183	**31**	6
	182	**32**	10
2015	**183**	**32**	13
	183	**31**	12
	182	**32**	14
Sum			**93**

2.3 Satellite Data Processing

2.3.1 C2RCC Processor

The C2RCC outputs results for Chl-a and TSM concentration, however algorithm execution demands additional background information, such as water surface salinity, elevation, ozone, water surface temperature, and air pressure. To increase the accuracy of the processor, salinity and temperature values were used from previous in situ measurements. Values for the surface ozone layer and air pressure were retrieved from the ERA5 model, a fifth generation ECMWF atmospheric reanalysis dataset of the global climate, covering the period from January 1950 to present and providing hourly estimates in a large number of atmospheric, land and oceanic climate variables, with 30km spatial resolution.

2.3.2 The Takagi-Sugeno neuro-fuzzy model

A fuzzy model is a non-linear method aiming to create a quantitative model utilizing data collected from complex phenomena. A series of "IF-THEN" rules help to define the mapping of inputs to outputs. A rule is made up of input and output variables and adjectives such as “low” and “high” that identify those variables. Before constructing a Takagi–Sugeno-rule-based fuzzy inference system, all the terms should be defined together with the adjectives that describe them.

In this study, a Takagi-Sugeno neuro-fuzzy model was developed aiming to inter-calibrate the Chl-a concentration values. A database of 130 in-situ Chl-a concentration values were associated with the respective reflectance values from bands 4 to 7 of Sentinel 2 and bands 1 to 5 of Landsat 8. 60% of data from the database were used for training the Takagi-Sugeno neuro-fuzzy model, 20% for model validation and 20% for model testing. The model was implemented in Matlab 2018, utilizing the standard Adaptive Neural Fuzzy Inference System (ANFIS) algorithm. Initially, the fuzzification of input values (4 antecedents: reflectances at each band; 1 output: log(Chl-a)) through the general bell-shaped membership function and the grid partition method, led to the definition of membership values in the three fuzzy sets (“low”, “medium”, “high”). Then, a series of multiple-input–single output fuzzy rules were applied of the form: if band1 is “LOW” AND band2 is “MEDIUM” AND band3 is “LOW” and band4 is “HIGH” then log(Chl-a) = f(band1, band2, band3, band4). Finally, the evaluation and weighting of the basis functions and the final evaluation of the output Chl-a value were followed in the defuzzification step.

Model testing error analysis exhibited the following metrics: Mean Squared Error = 0.000018; Root Mean Squared Error = 0.00418; r2 = 0.996 for Sentinel 2 and Mean Squared Error = 0.000043; Root Mean Squared Error = 0.00659; r2 = 0.925 for Landsat 8.

Figure 4 presents the distribution of the three fuzzy sets per Sentinel 2 band.

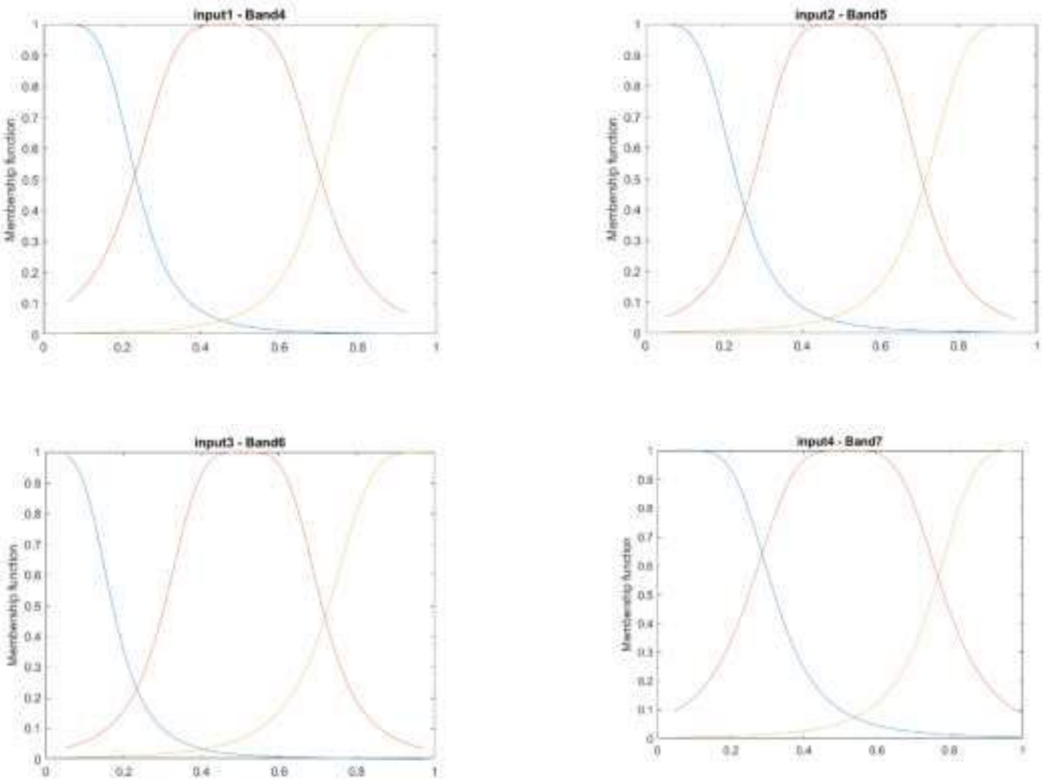

Figure 4. The fuzzy sets per Sentinel 2 band.

All input data, along the x-axis of the following diagrams, were normalized prior the neuro-fuzzy implementation. The y-axis represents the degree of membership of each input value into a specific fuzzy set.

Figure 5 illustrates the variation in the training and testing errors, between the observed and modelled values throughout the model iterations. It occurs that after a certain number of iterations the training error remains stable at very low levels (0.001 0.004 mg/m^3) while the testing error converges towards 0.004 mg/m^3. Figure 6 depicts the change of the prediction error over the iterations performed by the TS neuro-fuzzy model.

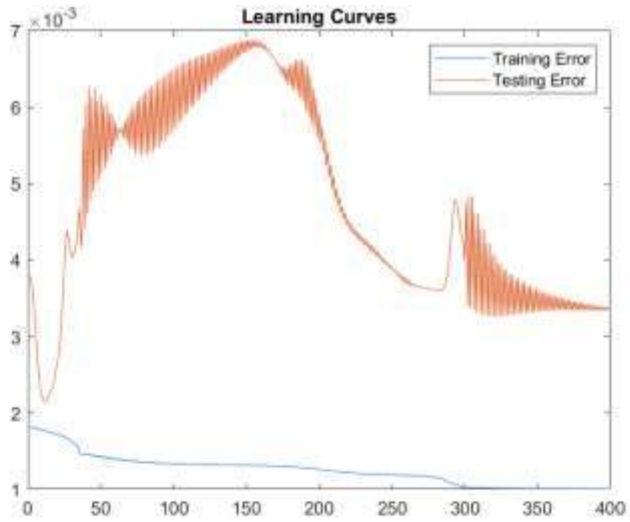

Figure 5. The variation of the training prediction error with the number of model iterations.

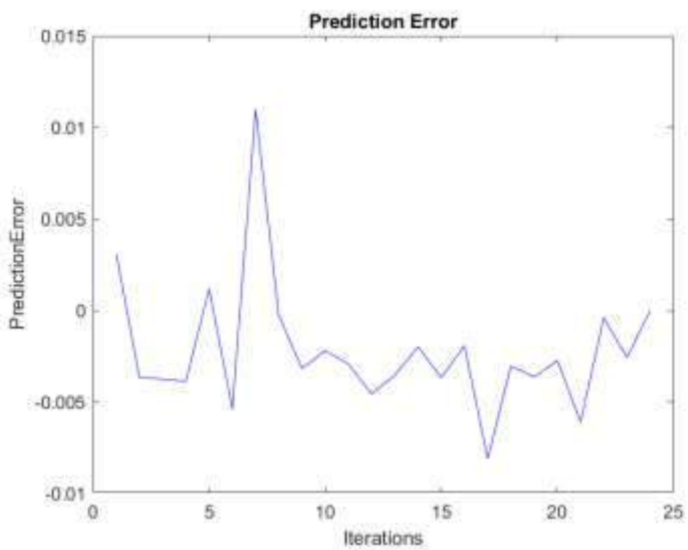

Figure 6. The variation of the prediction error with the number of model iterations.

2.3.3 The PONTOS Methodological Framework

Figure 7 describes the methodological framework of PONTOS eutrophication assessment and monitoring. Sentinel 2 and Landsat 8 satellite images were collected for the study area and period. All images were stored on the local DUTH server purchased from PONTOS project for that purpose. Satellite images were imposed on subsetting, atmospheric correction and resampling. Chl-a data were derived using the Takagi-Sugeno neuro-fuzzy model and maps of surface Chl-a concentration distribution were created. Furthermore, data were statistically analyzed, frequency distributions per lagoon were examined and threshold Chl-a levels for the identification and warning of extreme eutrophic events and blooms were established. Probability density functions and cumulative density functions were fitted on the histograms and the probability of threshold exceedance per lagoon and per lagoon's specific zone were assessed. Maps of probability for threshold exceedance were created illustrating areas vulnerable and prone to eutrophication.

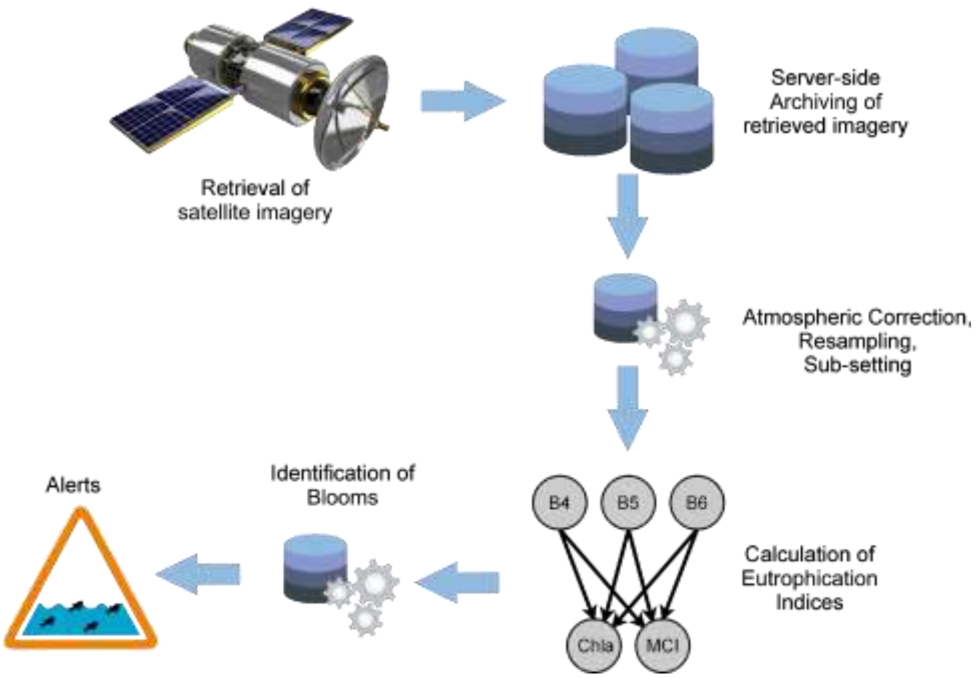

Figure 7. The PONTOS methodological framework for eutrophication assessment.

2.4 Eutrophication Assessment

Several trophic conditions classification schemes have been proposed in the literature to assess the environmental state of aquatic systems in terms of nutrients recycling. More complete trophic classification schemes are based on nutrients (phosphates, nitrates, ammonium), chlorophyll-a and total number of phytoplankton cells. Aquatic systems are classified into oligotrophic, lower mesotrophic, higher mesotrophic and eutrophic and ranges are given per parameter. Nutrient concentrations are given in μM, phytoplankton cells number in cells/l and chlorophyll in μg/l.

Table 6. Classification of aquatic systems according to their trophic conditions.

Parameter	Oligotrophic	Lower mesotrophic	Higher mesotrophic	Eutrophic
Phosphates (PO4) (μM)	<0.07	0.07-0.14	0.14-0.68	>0.68
Nitrates (NO3) (μM)	<0.62	0.62-0.65	0.65-1.19	>1.19
Ammonium (NH4) (μM)	<0.55	0.55-1.05	1.05-2.20	>2.20
Phytoplankton (cells/l)	$<6.0\times10^3$	6.0×10^3-1.5×10^5	1.5×10^5-9.6×10^5	$>9.6\times10^5$
Chlorophyll-a (μg/l)	<0.10	0.10-0.60	0.60-2.21	>2.21

The scheme above introduces a scale with four levels of eutrophication: eutrophic, higher mesotrophic, lower mesotrophic and oligotrophic, though 5 classes are required for WFD.

To achieve this harmonization, a new eutrophication scale was proposed by Karydis (1996) and Simboura et al. (2005), to comply with the ecological status levels described in WFD.

To process the satellite-derived Chl-a data, a chlorophyll multimetric is proposed to incorporate compliance assessment of five statistics in chlorophyll biomass:

- mean
- median
- percentage compliance over a threshold (10 μg/l Chl)
- percentage compliance over a threshold (20 μg/l Chl)
- percentage exceedance over a maximum threshold (50 μg/l Chl).

Estimates for the chlorophyll-a multimetric are proposed to delineated into two salinity zones, inner (salinity 1 - 25) and outer (salinity > 25), with thresholds for assessing compliance of the statistics, for each specific salinity zone.

To assess the percentages exceeding a certain threshold value, historic Chl-a data derived from satellite images were collected at specific sites, representing diverse conditions within each lagoon. These data were used to assess the probability of exceedance of a certain Chl-a level. Several probability density functions are available in the literature to be fitted on these Chl-a distributions. Therefore, on the Chl-a frequency histogram the best theoretical probability density function was fitted. The AIC and BIC minimization served as the criteria to select the most appropriate fitting model and assess the probability of Chl-a eutrophication threshold exceedance, set at 2 mg/m^3.

2.5 Study Site Description

2.5.1 The Greek Pilot area (PONTOS-GR)

The Greek Pilot area consists of 3 lagoons that belong to the Nestos complex (Vassova, Eratino and Agiasma lagoon), one located in Xanthi Prefecture (Porto-Lagos lagoon) and two in Rodopi Prefecture (Xirolimni and Ptelea lagoon) (Figure 8). All these lagoons are ecologically important sites, part of the East Macedonia and Thrace National Park and protected by the Convection on Wetlands of International Importance (Ramsar Convention) (Tsihrintzis et al., 2007).

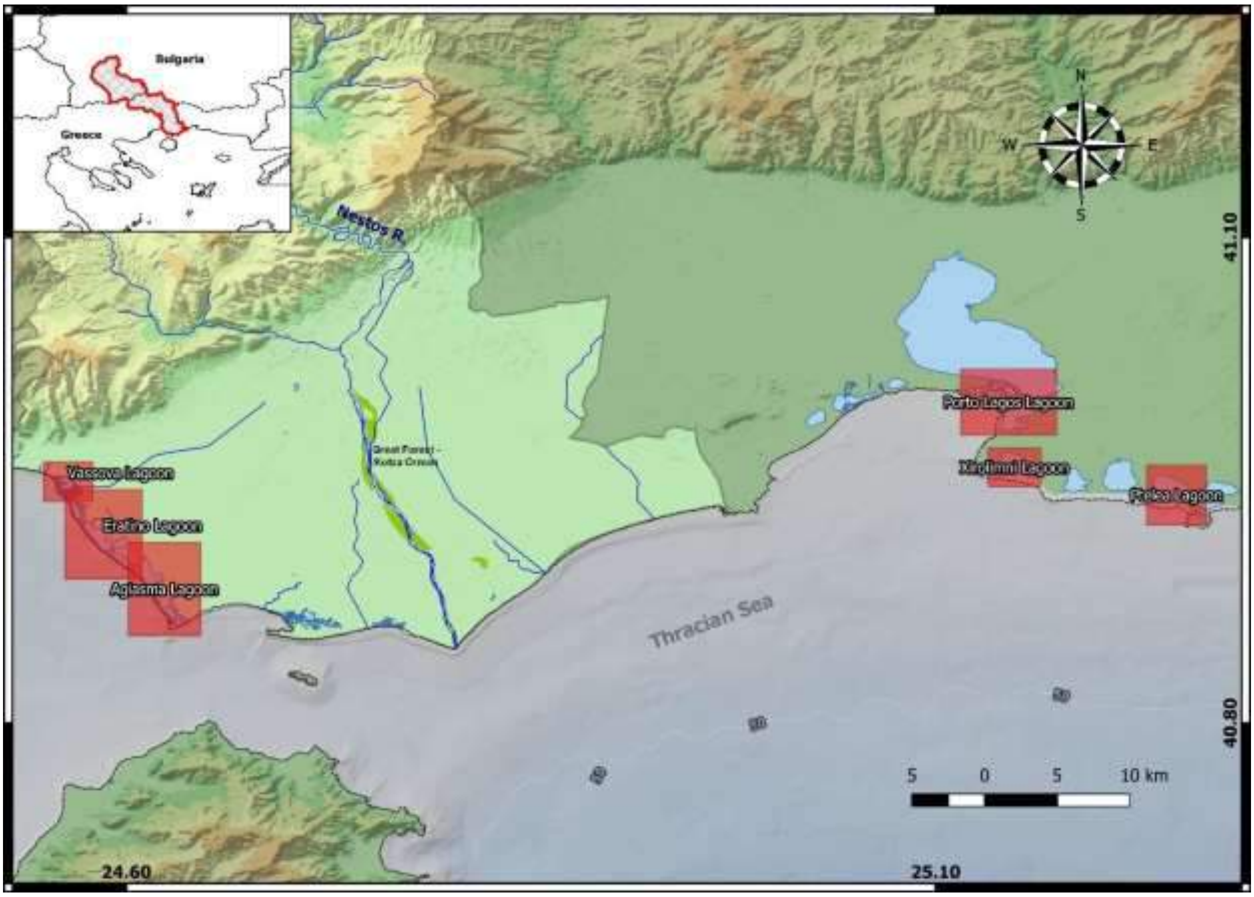

Figure 8. Lagoons under study.

2.5.1.1 *Vassova lagoon*

Vassova lagoon is a small in size (2.7 km^2) and shallow (mean depth: 0.8 m) coastal lagoon located at the western bank of river Nestos (Figure 9). The lagoon consists of a central main basin used for extensive aquaculture, and 16 dredged wintering canals, ranging from 30 to 50 m long and 0.5 m deep each. Vassova lagoon may be considered as a closed system, i.e., there is no freshwater input except directly from rainfall and through seepage from the adjoining agricultural lands. The lagoon is connected to the open sea (Kavala Gulf, North Aegean Sea) with an inlet channel approximately 15 m wide, 200 m long and 0.7 – 0.8 m deep at mean sea level. This lagoon is ecologically important providing water-fowl habitat, and is also exploited for fish production (30 tn/year) (Sylaios et al., 2006).

Figure 9. Vassova lagoon.

2.5.1.2 Eratino lagoon

Eratino Lagoon is approximately 2.9 km^2, with a length of about 5.9 km, average width of 0.7 km (maximum width of 1.5 km) and a perimeter of 43 km (Figure 10). The mean depth of the lagoon is 0.8 m and the maximum depth 3.4 m. The lagoon is connected to the open sea (Kavala Gulf) with two inlet channels and it communicates with Vassova lagoon through a narrow, shallow channel (Tsihrintzis et al., 2007). Eratino receives fresh water by a natural channel in the northern part of the basin and agricultural runoff by direct drainage (Sylaios and Theocharis, 2002).

Figure 10. Eratino lagoon.

2.5.1.3 Agiasma lagoon

Agiasma, a shallow lagoon with a mean depth of 0.5 m, covers an area of 3.3 km^2, with a length of about 7 km, a mean width of 0.8 km and a perimeter of 24.3 km. It is connected with the sea with two narrow outlets (Figure 11). The outlet in the middle of the basin remains open during stocking, from mid-February to May, while the outlet in the south part of the lagoon is always open. Agiasma is considered to be one of the less affected by eutrophication system of the Nestos Delta complex (Orfanidis et al., 2008).

Figure 11. Agiasma lagoon.

2.5.1.4 Porto Lagos lagoon

Porto Lagos is a shallow coastal lagoon, with a mean depth of about 0.5 m and covers an area of 3.75 km^2 (Figure 12). It is connected to Vistonis Lake through three short channels (50 m long and 25 m wide) and to Vistonikos Gulf (Thracian Sea, Northern Aegean Sea) through a channel 60 m wide and 600 m long. It is a micro-tidal environment with tidal range less than 0.30 m during spring tides. Wave action is negligible and water circulation allows for the sufficient oxygenation of the lagoon. Water is generally turbid; highest turbidity was observed during the warmest months. The lagoon bottom is regular, covered by soft mud and sand on the periphery. Salt marshes, mudflats and sandflats border the lagoon. Seagrasses constitute the majority of submerged aquatic vegetation (Koutrakis et al., 2005).

Figure 12. Porto-Lagos lagoon.

2.5.1.5 *Xirolimni lagoon*

Xirolimni lagoon has an average depth of 0.6 m covering an area of 1.8 km^2 and is located on the western side of the Fanari settlement (Figure 13). It connects to the sea with a narrow, 320 m long outlet. Xirolimni receives fresh water from precipitation and direct runoff.

Figure 13. Xirolimni lagoon.

2.5.1.6 Ptelea lagoon

Ptelea is a shallow system with an area of 3.6 km^2. It communicates with Elos lagoon from the East and with the Thracian Sea through a narrow inlet (Figure 14). Both Xirolimni and Ptelea are located within an agricultural watershed and they receive fresh water from precipitation or direct drainage.

Figure 14. Ptelea lagoon.

All six lagoons are surrounded by permanent cultivated areas (mostly cotton, maize, alfalfa), which leads to receiving agricultural runoff especially during flash flood events. Lagoons are forced by similar tidal influence (spring tidal range 0.4 m and neap tidal range 0.2 m) at their mouths and they belong to the same Koppen climatic zone (Csb, warm summer Mediterranean climate). Mean annual precipitation is around 320 mm ranging between 420 – 430 mm and air temperature between -5-38 °C with mean temperature around 15 °C. In North Aegean Sea, winds blowing from the north and northeast dominate, while south-southwestern winds prevail in spring and summer. The geometric and hydrologic parameters for the six lagoons are summarized in at **Table 7**.

Table 7. Study sites and their Geometric and hydrologic characteristics.

Lagoon	Geographical boundaries	A (km^2)	h (m)	V (km^3)	Perimeter (km)
Vassova	24.552° A, 40.929° B : 24.569° A, 40.957° B	2.70	0.80	3.00×10^{-3}	5.25
Eratino	24.566° A, 40.894° B : 24.605° A, 40.938° B	2.88	0.77	2.23×10^{-3}	42.50
Agiasma	24.612° A, 40.853° B : 24.625° A, 40.913° B	3.33	0.50	1.66×10^{-3}	24.30
Porto-Lagos	25.133° A, 40.979° B : 25.168° A, 41.011° B	4.91	1.00	3.16×10^{-3}	40.00
Xirolimni	24.608° A, 40.861° B : 24.637° A, 40.903° B	1.76	0.52	0.90×10^{-3}	6.42
Ptelea	25.232° A, 40.923° B : 25.264° A, 40.964° B	3.60	0.80	2.90×10^{-3}	6.93

where A = lagoon surface area, h = mean lagoon water depth, V = lagoon water volume

3 Results

3.1 Spatial Chlorophyll analysis

By applying the Takagi-Sugeno neuro-fuzzy model, the spatio-temporal distribution of Chl-a concentration data were obtained and mapped. Satellite images for the period 2013-2021 were processed. Period 2013-2015 was covered by Landsat 8 images and period 2015-202I by Sentinel 2 images. Indicatively, a series of images throughout the years are presented, to show the seasonal evolution of Chl-a for each of the lagoons under study.

3.1.1 Vassova lagoon

Figures 12-21 show the spatial distribution of Chl-a in Vassova lagoon for the year 2013-2021. During 2013 (Figure 15), the highest Chl-a concentration values were reached in August. The increase started from the upper part of the basin and in the following summer months it moved to the central basin. In the autumn and winter months, the Chl-a values are decreased.

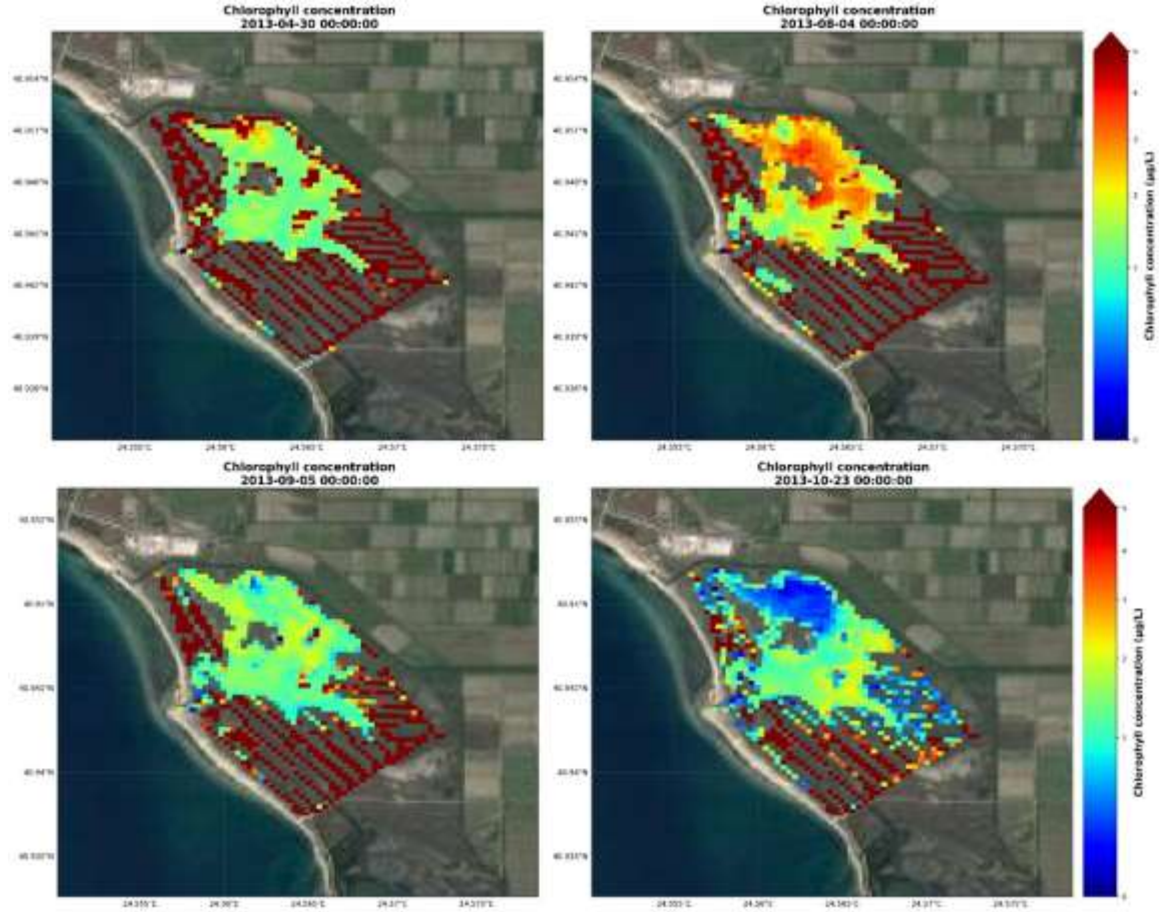

Figure 15. Seasonal evolution of Chl-a concentration in Vassova lagoon for the year 2013, based on Landsat 8 satellite images.

During 2014 (Figure 16), the Chl-a values were low from January to early July. Then they showed an increase at the northern part of the basin. The Chl-a values started to decrease in the following months.

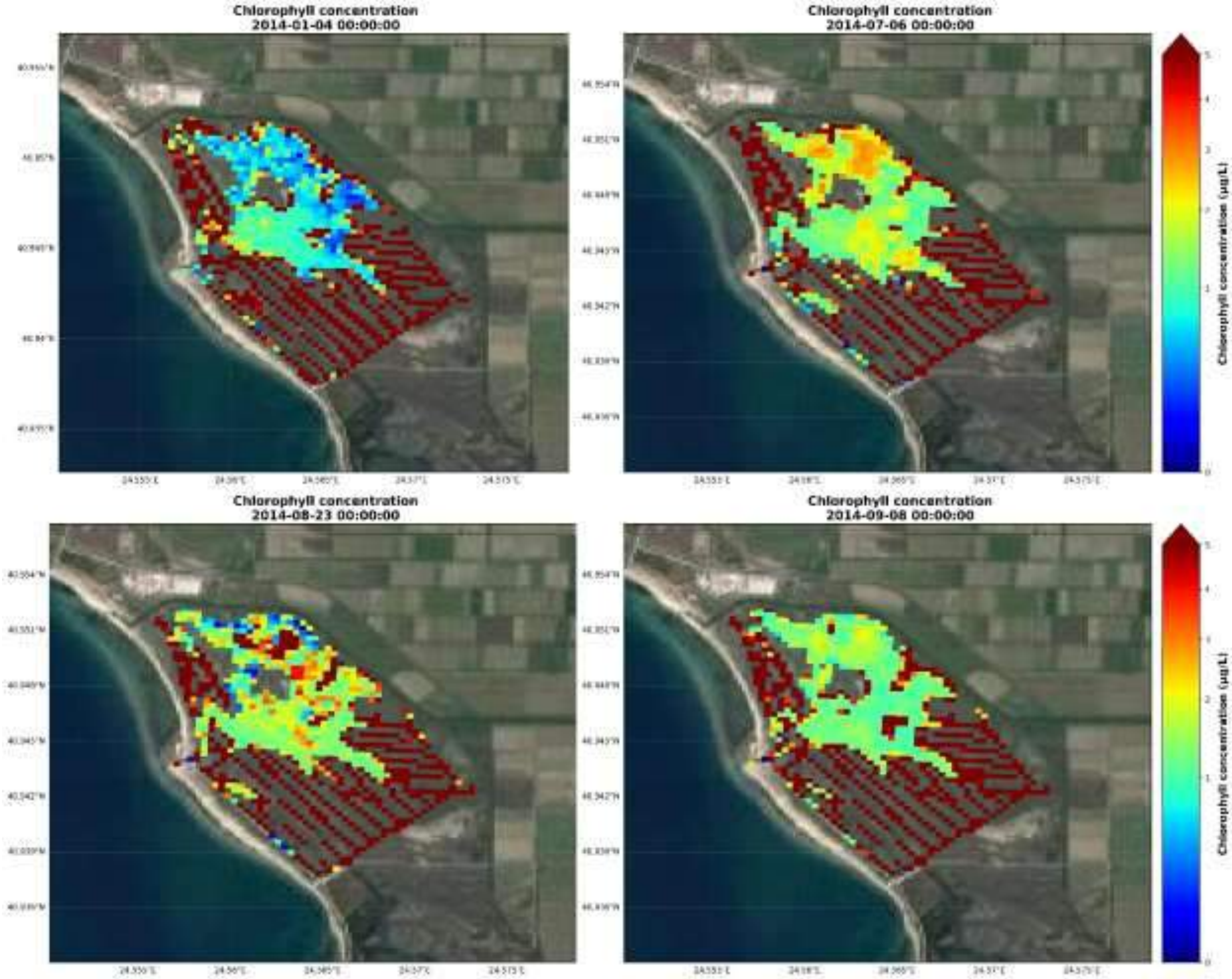

Figure 16. Seasonal evolution of Chl-a concentration in Vassova lagoon for the year 2014, based on Landsat 8 satellite images.

The first half of 2015 is presented in Figure 17 covered by Landsat 8 and the second half is presented in Figure 18 covered by Sentinel 2. During the first half of the year, Chl-a values decreased from January to February and then started increasing again until April.

Higher values are observed in the summer. At the end of the summer, Chl-a decreased until the end of the year, starting from the center of the basin and then spreading towards the coast.

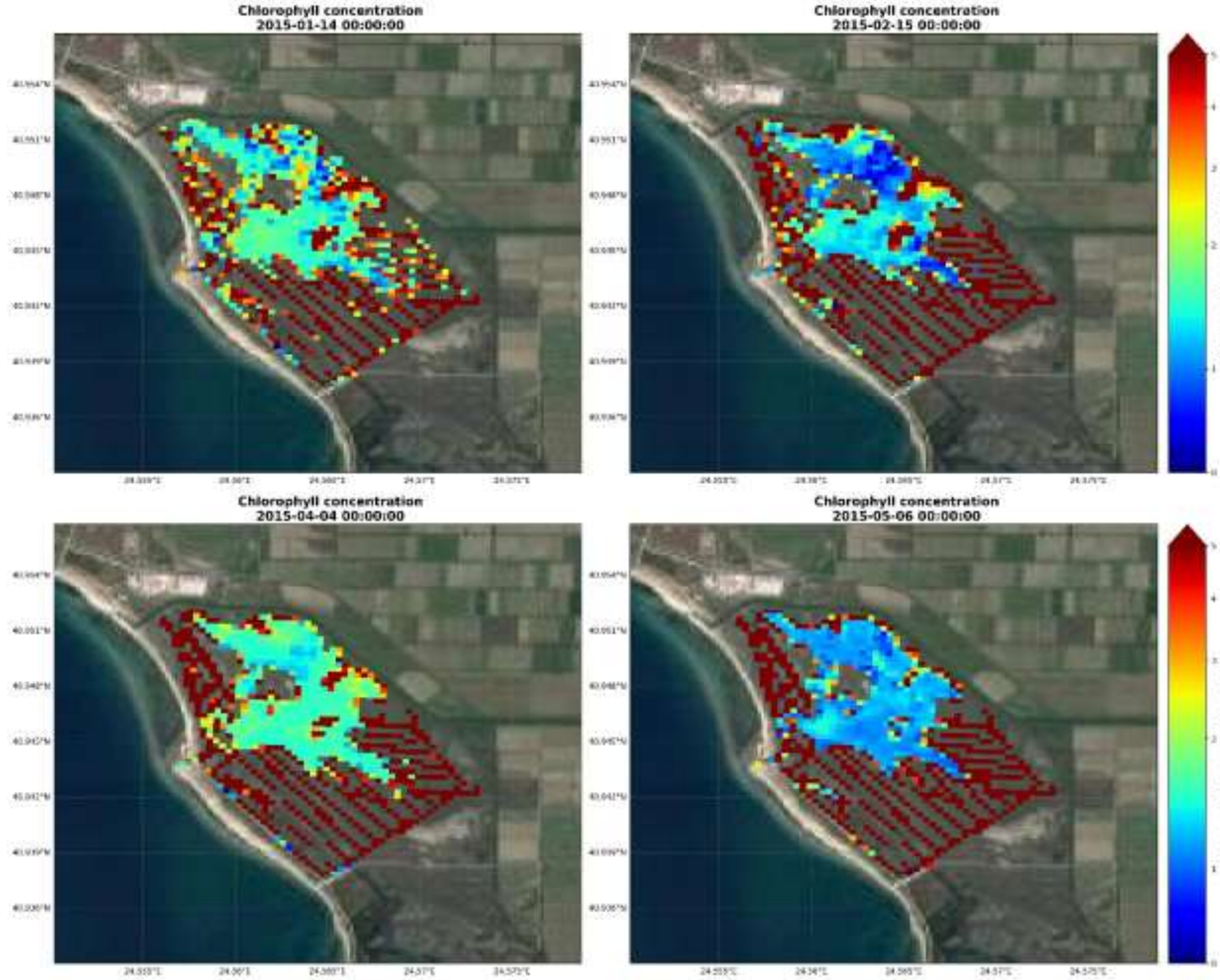

Figure 17. Seasonal evolution of Chl-a concentration in Vassova lagoon for the year 2015, based on Landsat 8 satellite images.

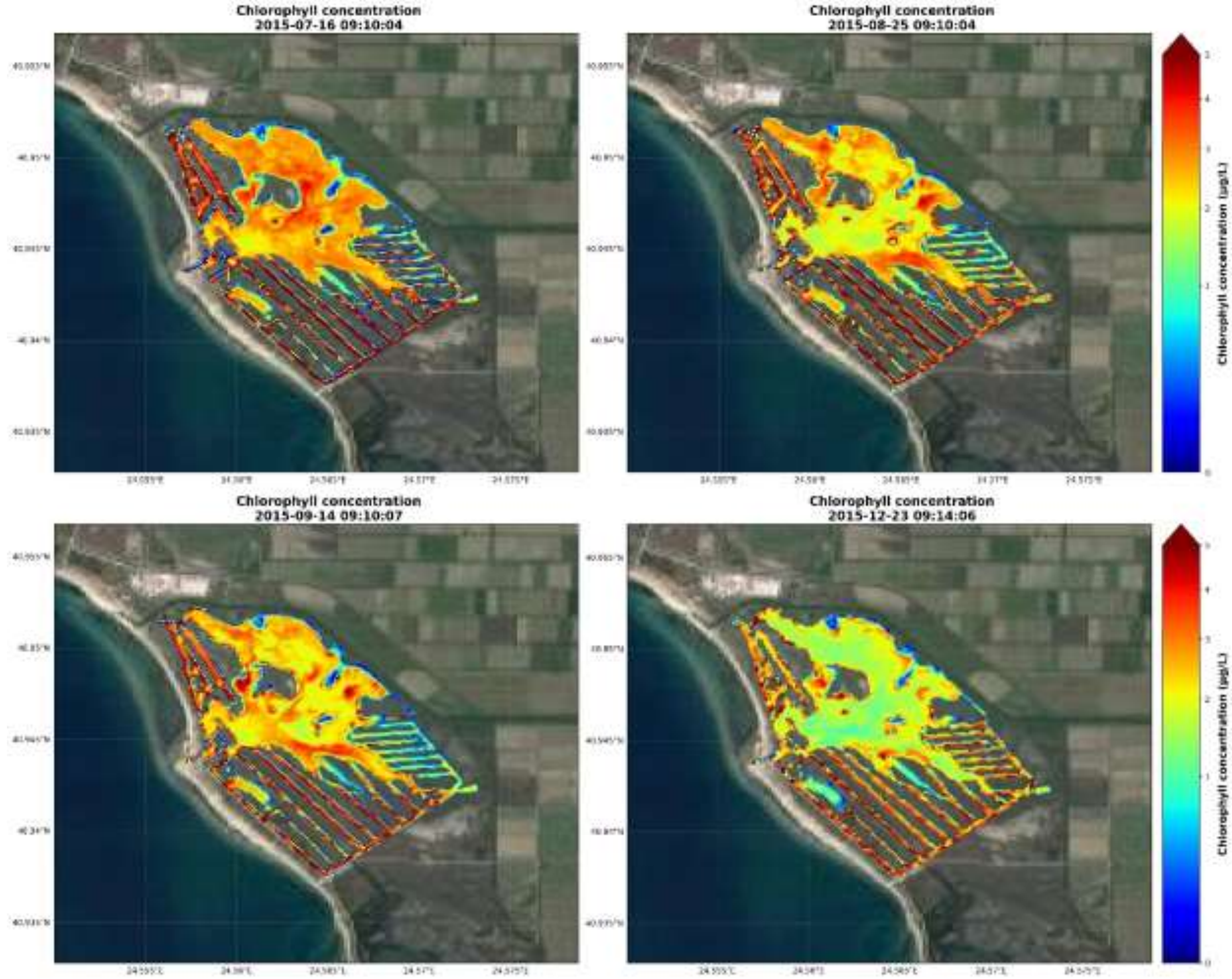

Figure 18. Seasonal evolution of Chl-a concentration in Vassova lagoon for the year 2015, based on Sentinel 2 satellite images.

The same pattern in Chl-a evolution is observed in 2016 (Figure 19), where the higher values are observed in the summer months and the decrease as we move on to the autumn and winter. The Chl-a values in the wintering canals increased in the summer and reached their highest values in September 2016.

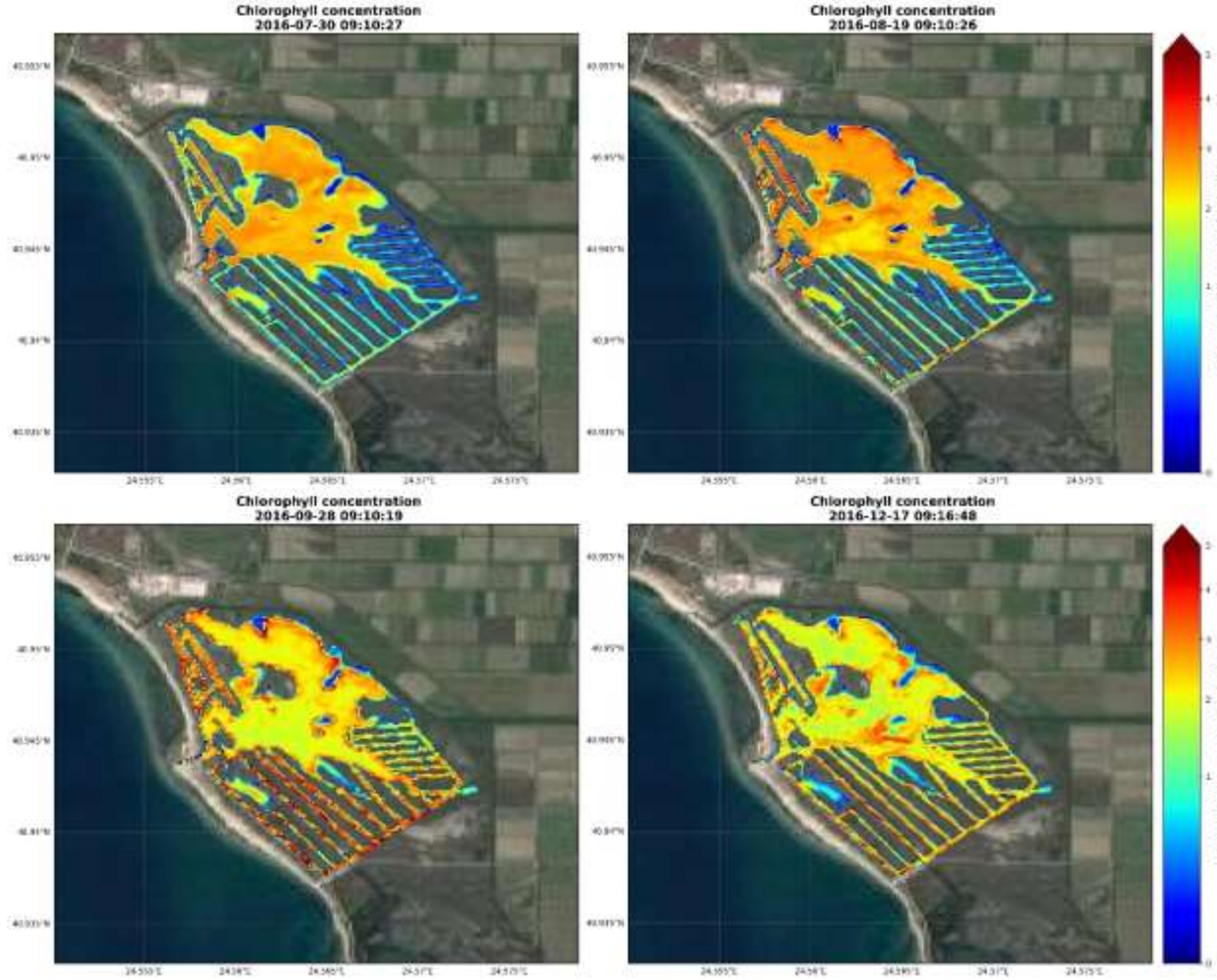

Figure 19. Seasonal evolution of Chl-a concentration in Vassova lagoon for the year 2016, based on Sentinel 2 satellite images.

Figure 20 shows the increase, from the low concentrations from the beginning of the year to the highest in June. The increase begins from the north and then expands to the rest of the basin. In the following months, Chl-a values decreased and then increased again, reaching their highest values in August. In the following months, Chl-a decreases until the end of the year.

The selected images for 2018 (Figure 21) show the increase of Chl-a values, from low concentrations at the beginning of the year until the summer, where the highest values occur in August. The highest values are observed at the center of the basin. In the following months, Chl-a values decrease until December.

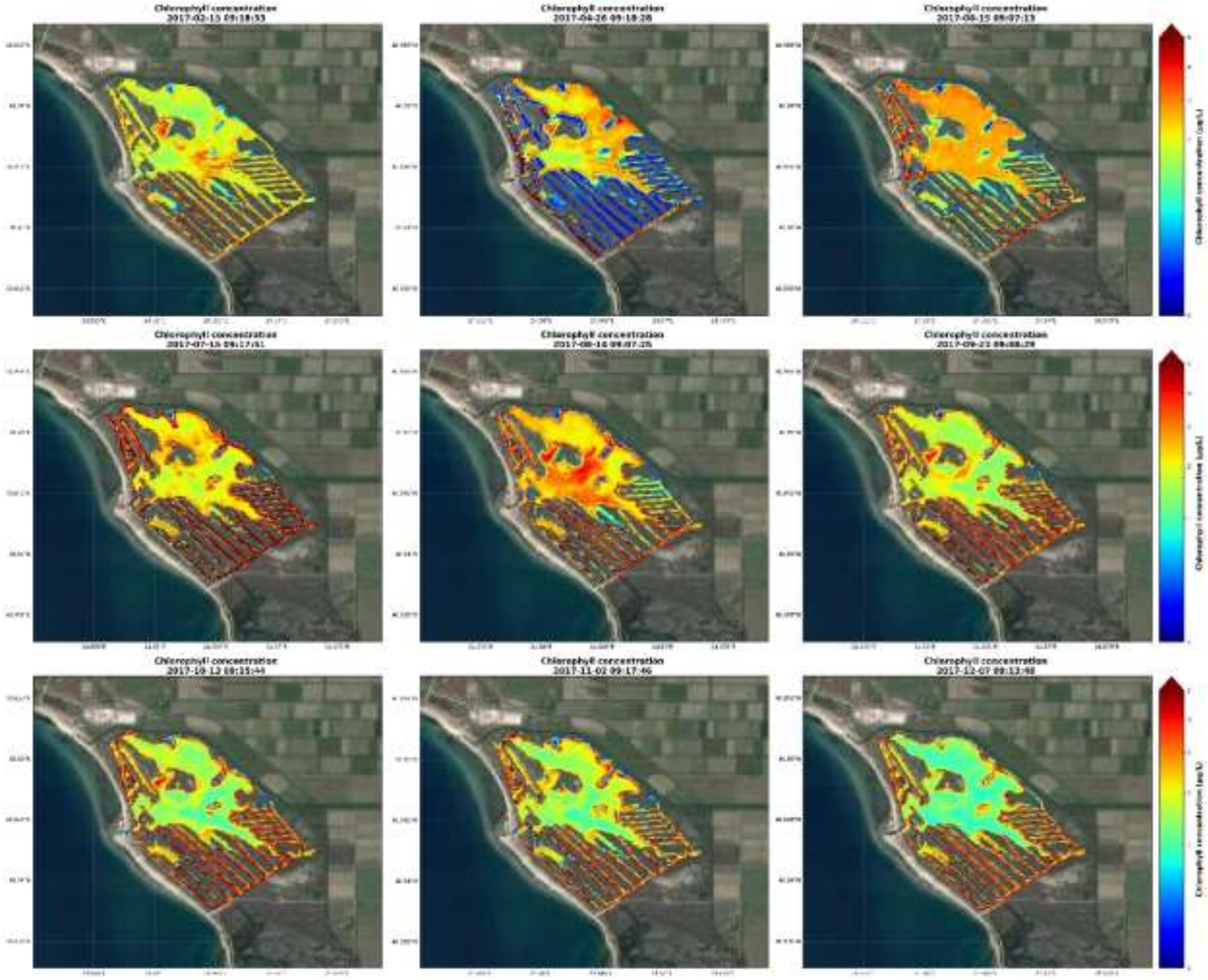

Figure 20. Seasonal evolution of Chl-a concentration in Vassova lagoon for the year 2017, based on Sentinel 2 satellite images.

Years 2019-2021 show a similar pattern in Chl-a values evolution (Figures 19-21). Initially, there is an increase of Chl-a values from January until August and after August, a decrease starts until the end of the year. The Chl-a increase starts from the north shore, then spreads to the center of the basin and ultimately to the wintering canals.

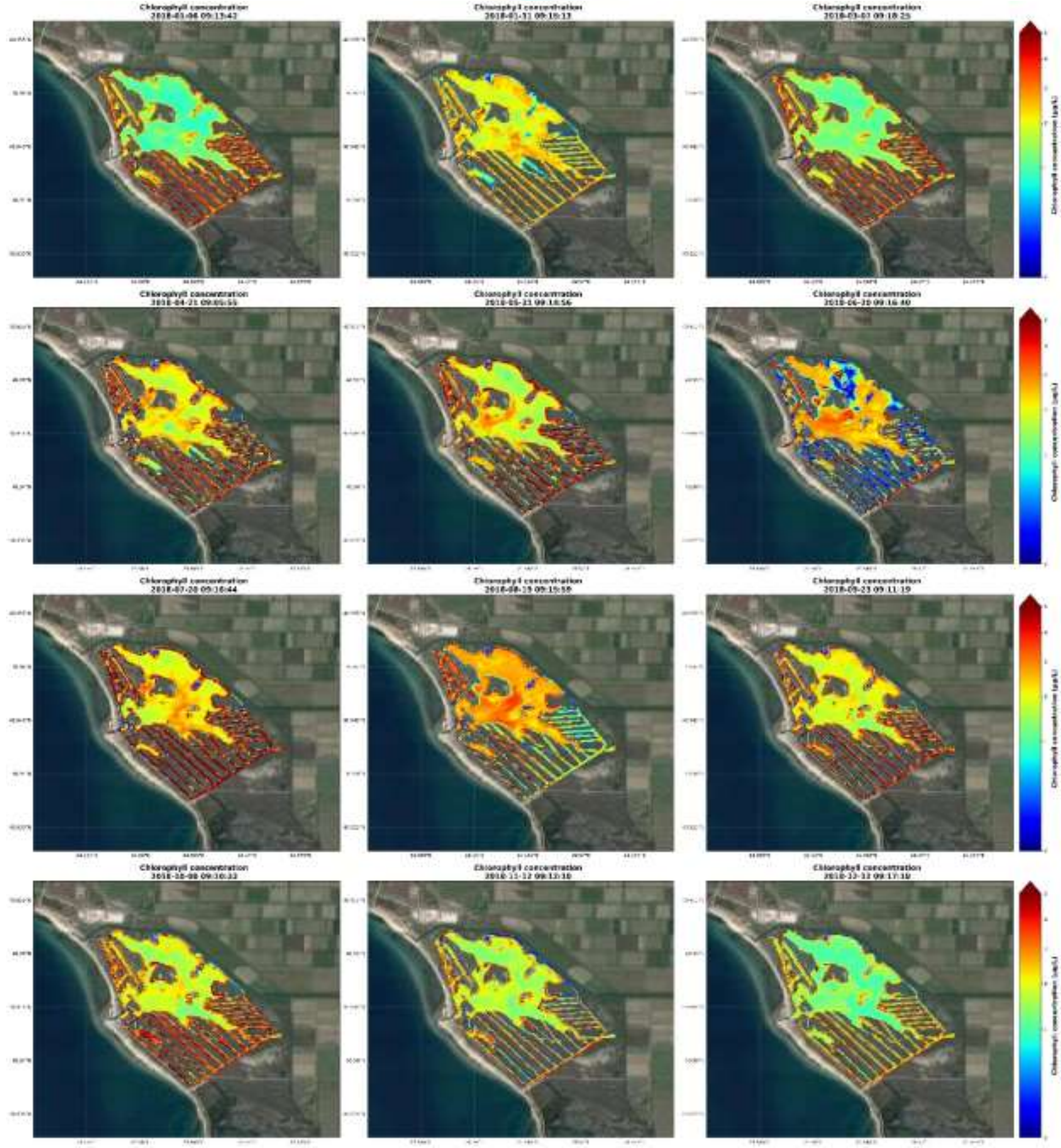

Figure 21. Seasonal evolution of Chl-a concentration in Vassova lagoon for the year 2018, based on Sentinel 2 satellite images.

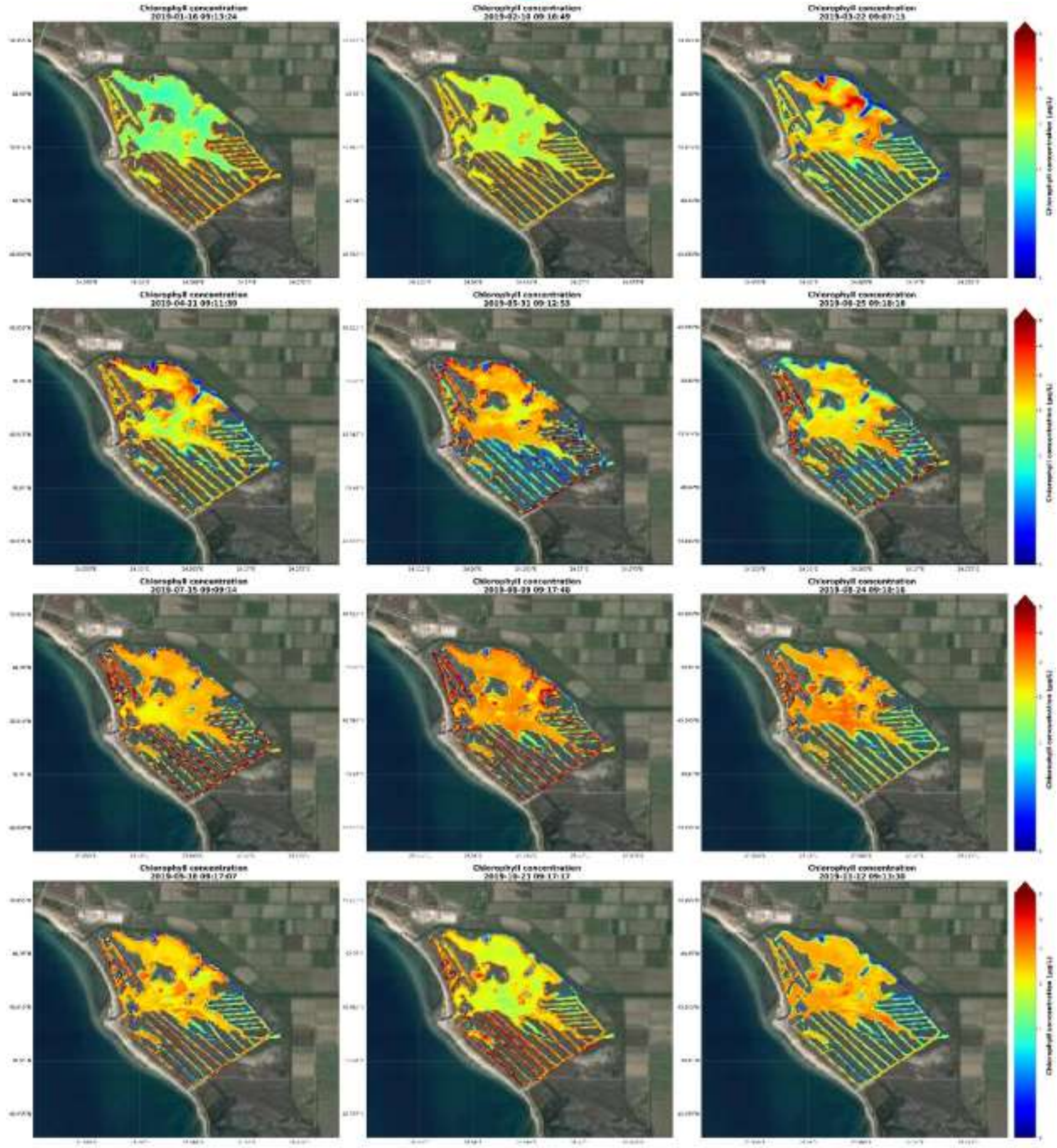

Figure 22. Seasonal evolution of Chl-a concentration in Vassova lagoon for the year 2019, based on Sentinel 2 satellite images.

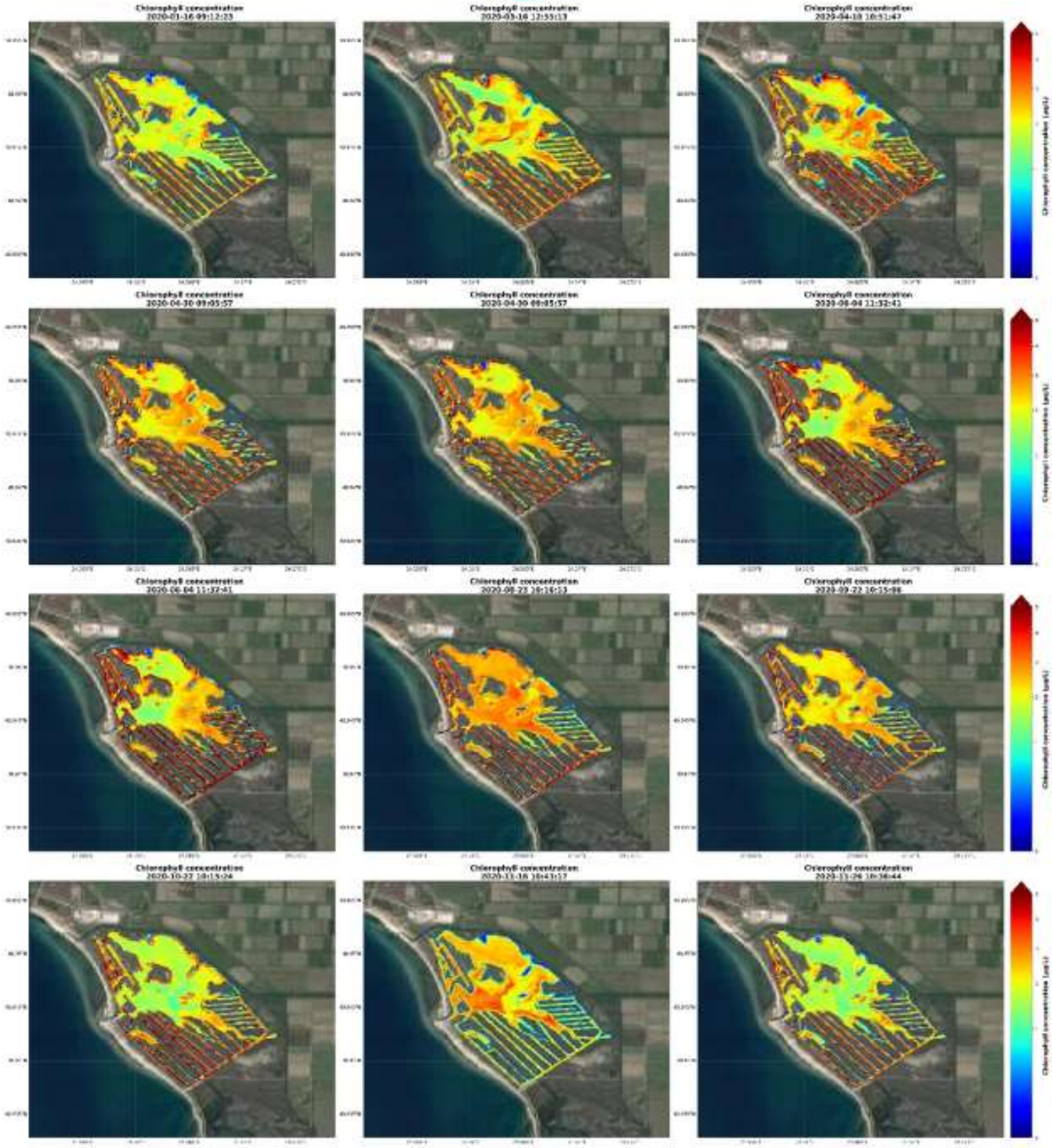

Figure 23. Seasonal evolution of Chl-a concentration in Vassova lagoon for the year 2020, based on Sentinel 2 satellite images.

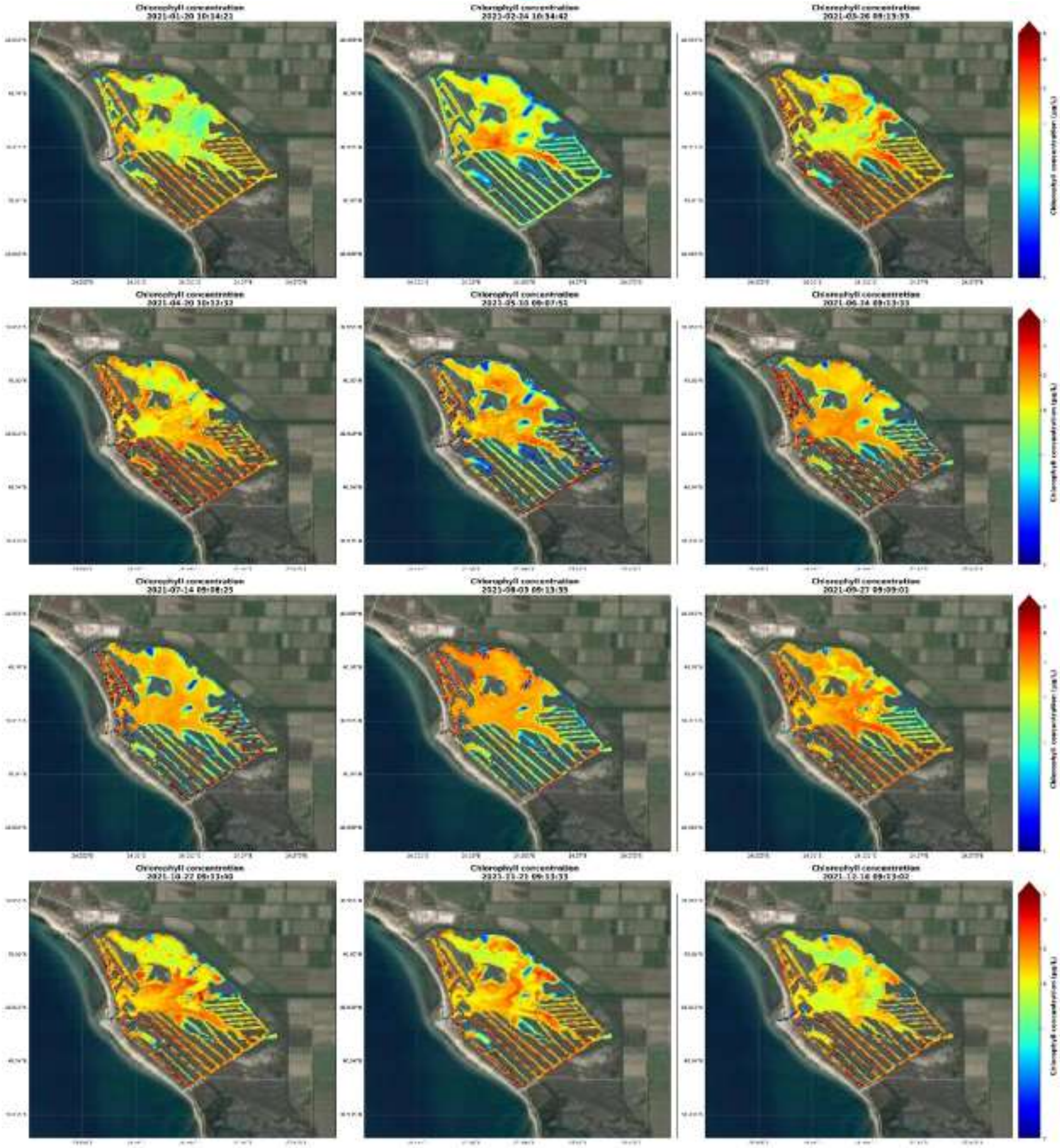

Figure 24. Seasonal evolution of Chl-a concentration in Vassova lagoon for the year 2021, based on Sentinel 2 satellite images.

3.1.2 Eratino lagoon

Figures 22-31 show the spatial distribution of Chl-a in Eratino lagoon for the years 2013-2021. During 2013 (Figure 25), the highest Chl-a concentration values were reached in July (up to 4.0 μg/l). The increase in Chl-a concentration started from the center of the basin and in the following summer months moved to the eastern and the southern parts of the lagoon.

In autumn and winter months, the Chl-a values decreased, with the northern and the southern parts having higher values than the center of the basin.

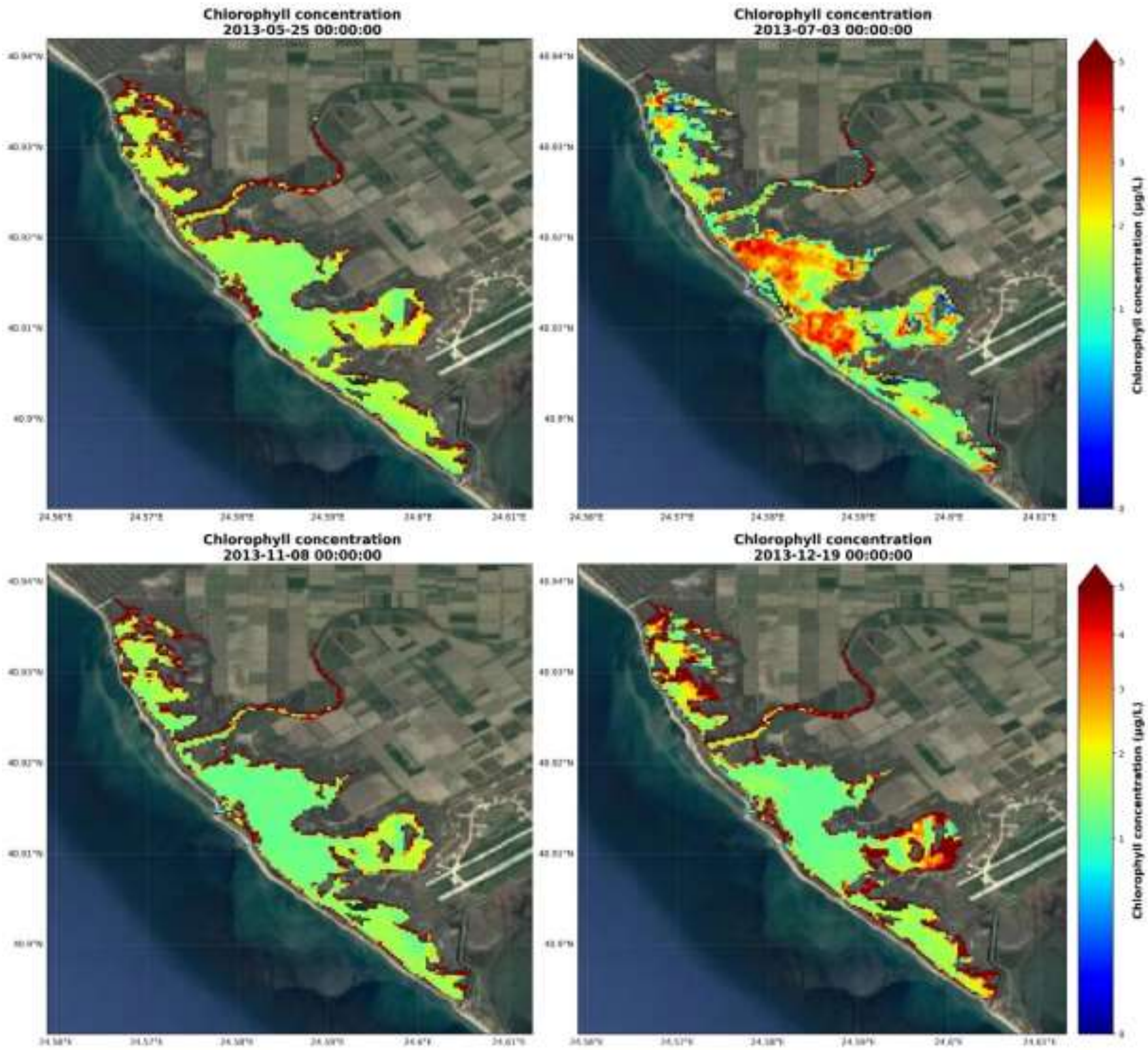

Figure 25. Seasonal evolution of Chl-a concentration in Eratino lagoon for the year 2013, based on Landsat 8 satellite images.

During 2014 (Figure 26), the Chl-a values were low from January to early July when they showed an increase at the northern part of the basin. The Chl-a values continued to increase and they reached the highest values in December 2014 (2.2 μg/l).

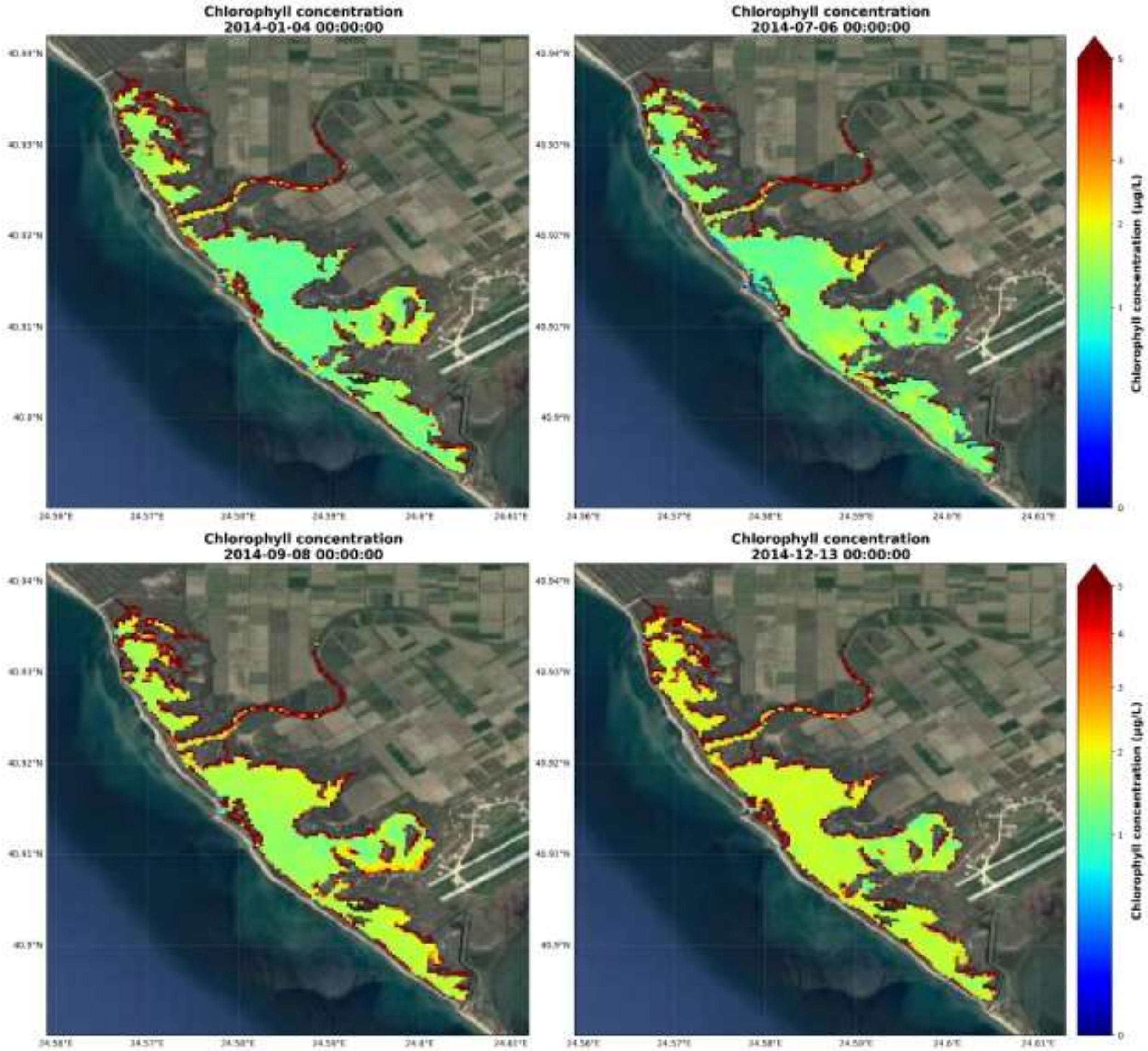

Figure 26. Seasonal evolution of Chl-a concentration in Eratino lagoon for the year 2014, based on Landsat 8 satellite images.

The first half of 2015 is presented in Figure 27 covered by Landsat 8 and the second half is presented in Figure 28 covered by Sentinel 2. The highest values were detected in December 2014, led to similarly high values in January 2015 (Figure 27). Chl-a values decreased from January to February and then started increasing again until April. In April the bottom part of the lagoon shows lower concentrations (1.0-2.0 μg/l).

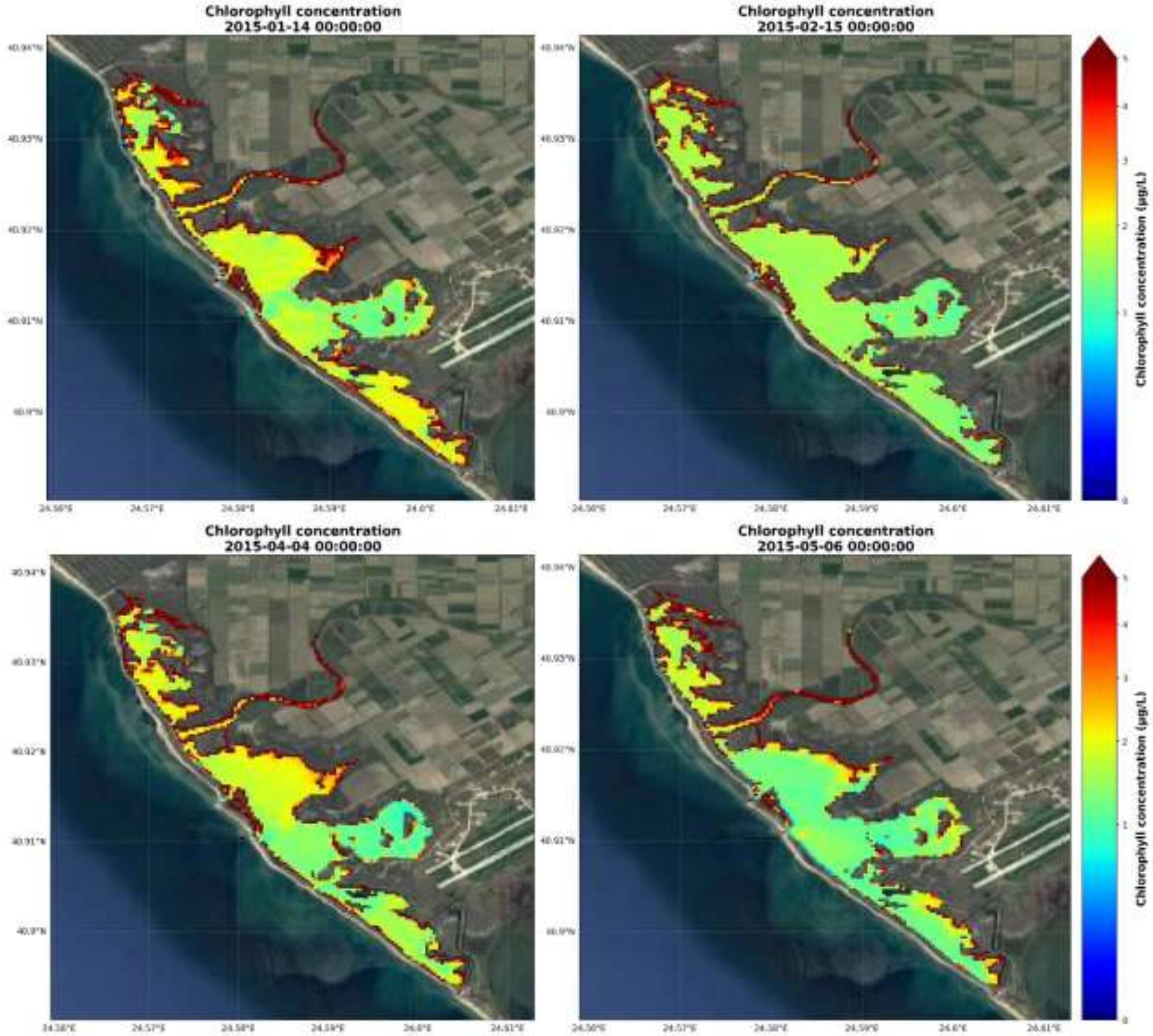

Figure 27. Seasonal evolution of Chl-a concentration in Eratino lagoon for the year 2015, based on Landsat 8 satellite images.

Figure 28 shows that the higher values are observed during the summer. At the end of the summer Chl-a deceased until the end of the year, with the exception of the southeast part, which seems to retain higher values compared to the rest of the basin.

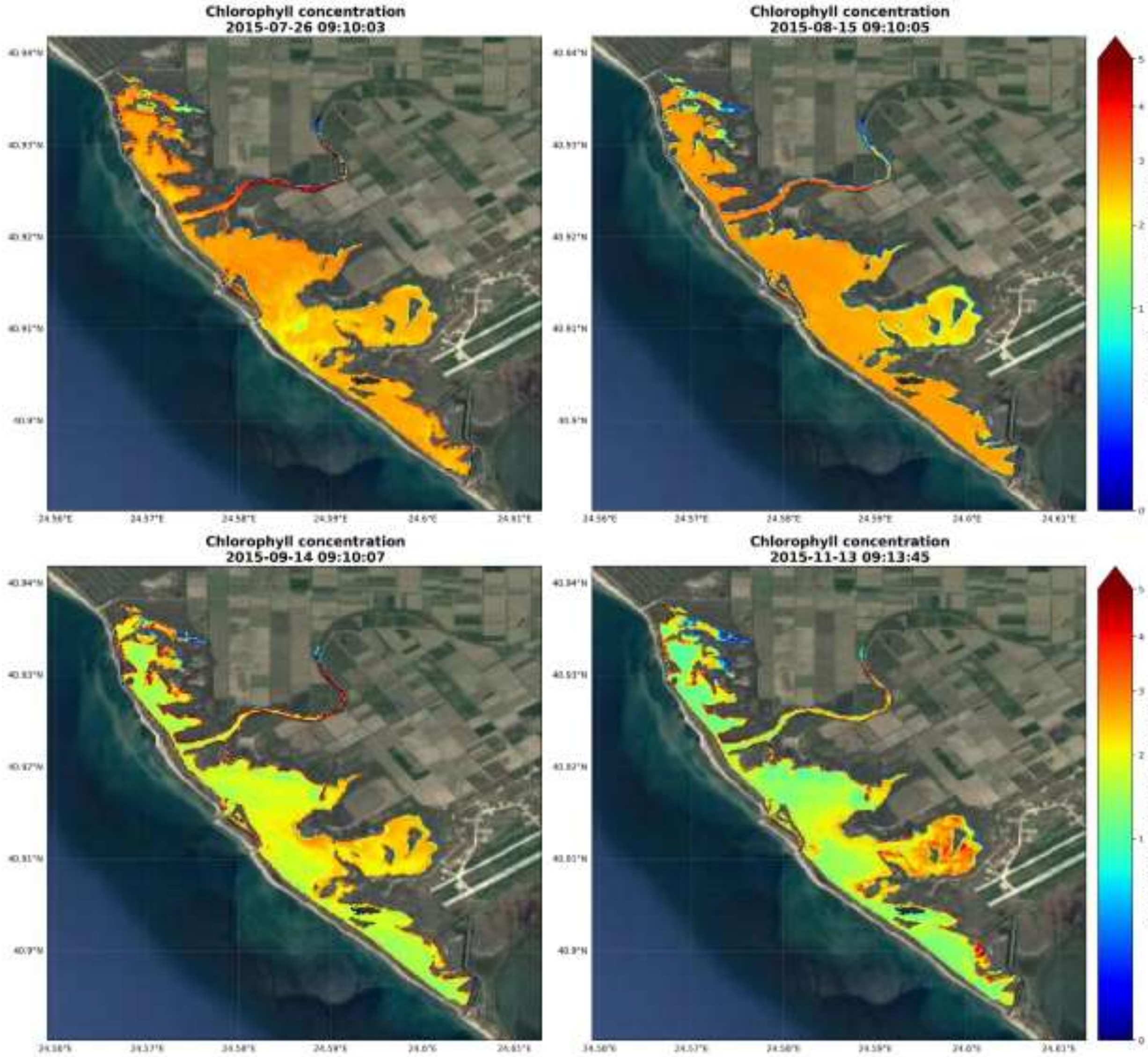

Figure 28. Seasonal evolution of Chl-a concentration in Eratino lagoon for the year 2015, based on Sentinel 2 satellite images.

The same pattern in Chl-a evolution is observed in 2016, where the higher values are observed in the summer months and they decrease as we move on to the autumn and winter. The higher values at the eastern parts in the autumn and winter months are also observed in 2016 (Figure 29).

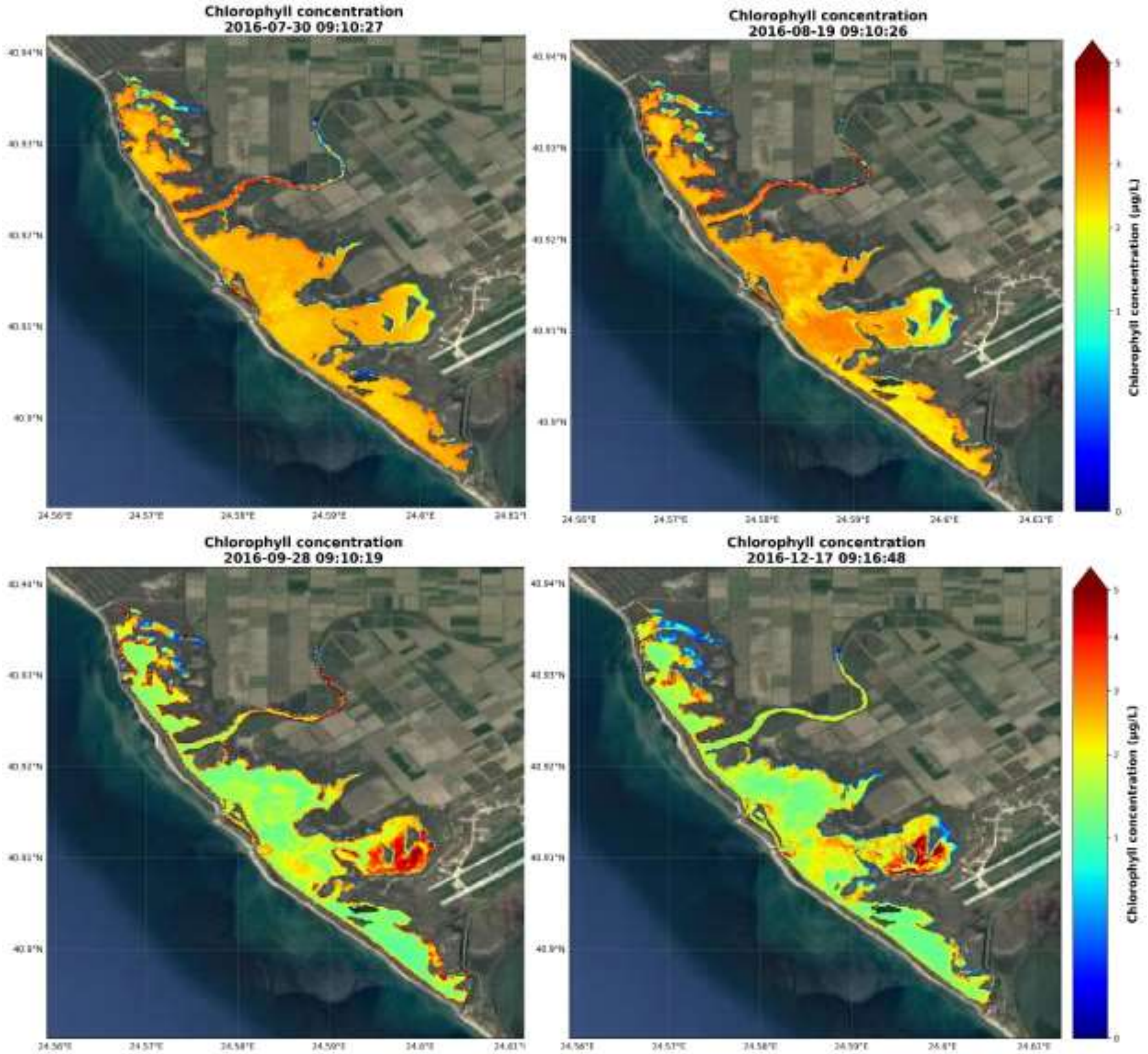

Figure 29. Seasonal evolution of Chl-a concentration in Eratino lagoon for the year 2016, based on Sentinel 2 satellite images.

Figure 30 shows the increase, from the low concentrations from the beginning of the year to the highest in June. The increase begins from the south and then expands to the rest of the basin. In the following months, Chl-a values decreased until the lowest level was reached at the end of autumn. At the end of December, a small increase in Chl-a is observed. The southeast part keeps showing higher values compared to the rest of the lagoon.

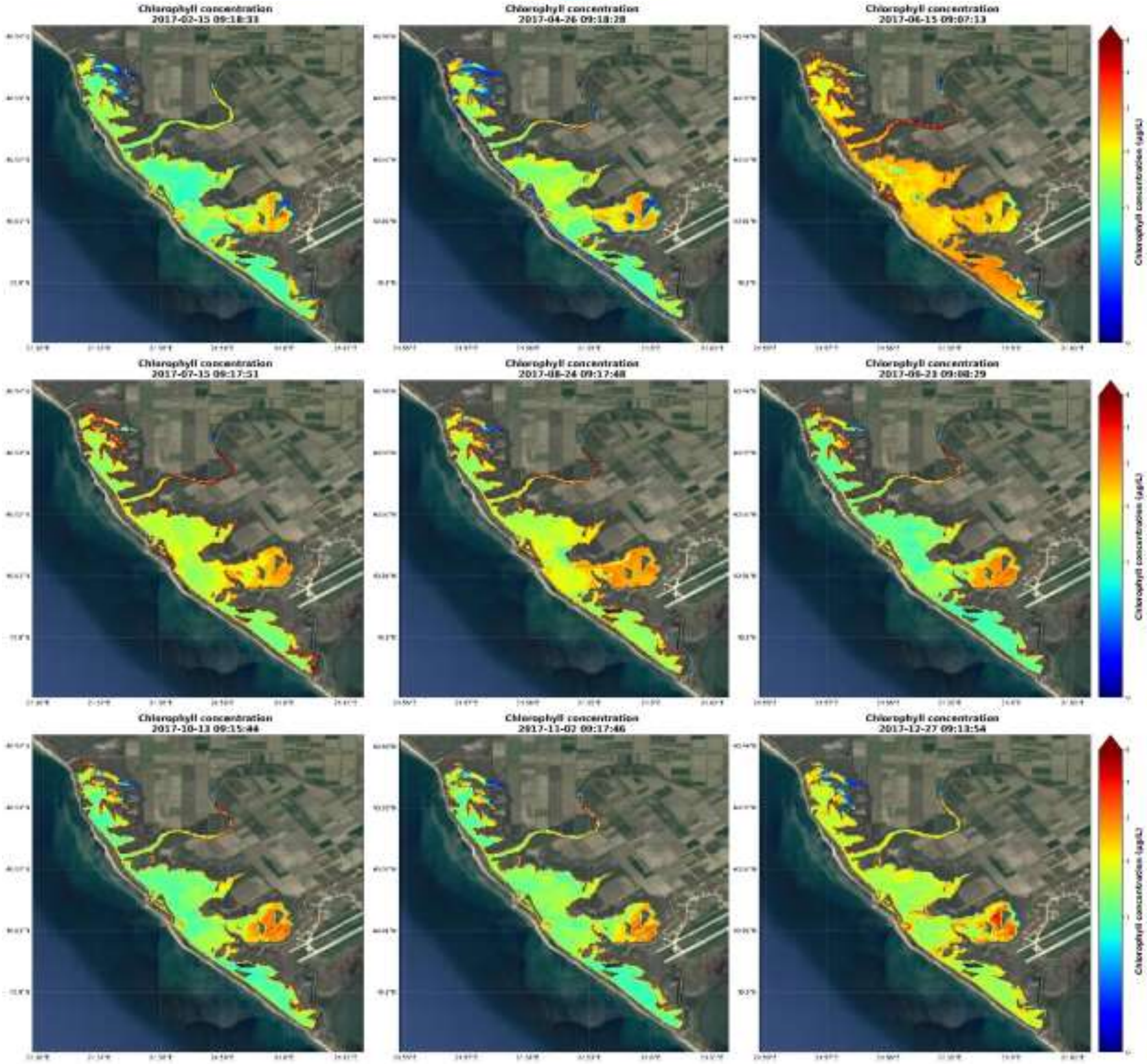

Figure 30. Seasonal evolution of Chl-a concentration in Eratino lagoon for the year 2017, based on Sentinel 2 satellite images.

Figure 31 shows the temporal and spatial evolution during 2018. Chl-a values are low at the beginning of the year and increase gradually until late May. The highest values are observed at the center of the basin. In the following months, Chl-a values decrease and then increase again until they reach the highest values at the end of the summer. Another peak is observed in November.

In 2019 (Figure 32), the first increase in Chl-a starts in late March and remains until late June. Then the Chl-a values slightly decrease in July and increase again in late August. The last maximum in Chl-a values is observed in November.

The slightly higher values detected in December 2019 led to high values in January 2020 (Figure 33). The first Chl-a peak is observed in March 2020 and concentration remains high until the end of the summer. The highest Chl-a values are reached in May 2020. Then Chl-a decreases until November. In mid-November, another maximum is reached (2.5-3.5 µg/l).

During 2021 (Figure 34), maximum Chl-a values are reached in February (2.5-3.5 µg/l) and then in May (2.5-4.5 µg/l). Higher values localize at the center part of the lagoon. In the following months, the Chl-a values decrease until the end of the year.

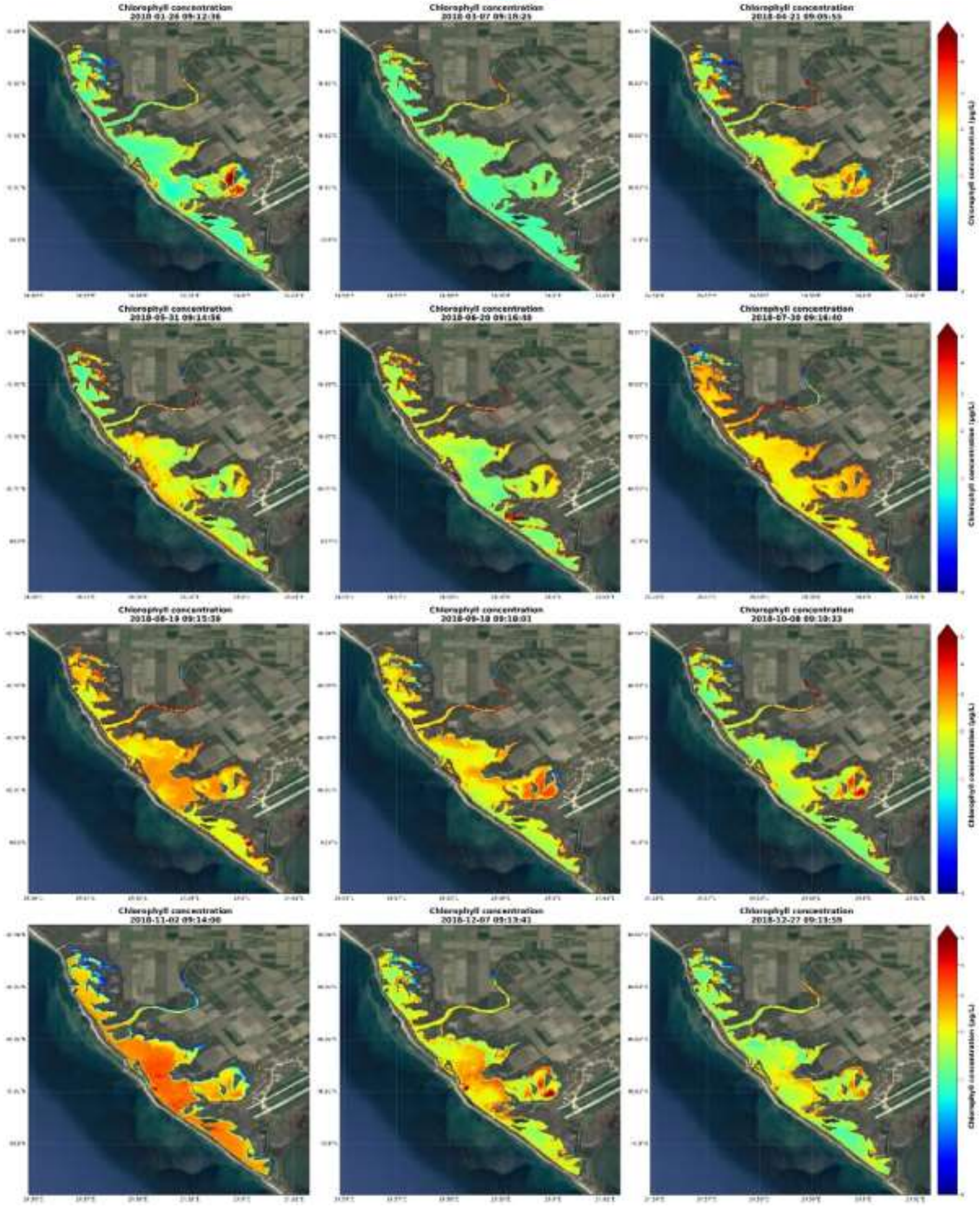

Figure 31. Seasonal evolution of Chl-a concentration in Eratino lagoon for the year 2018, based on Sentinel 2 satellite images.

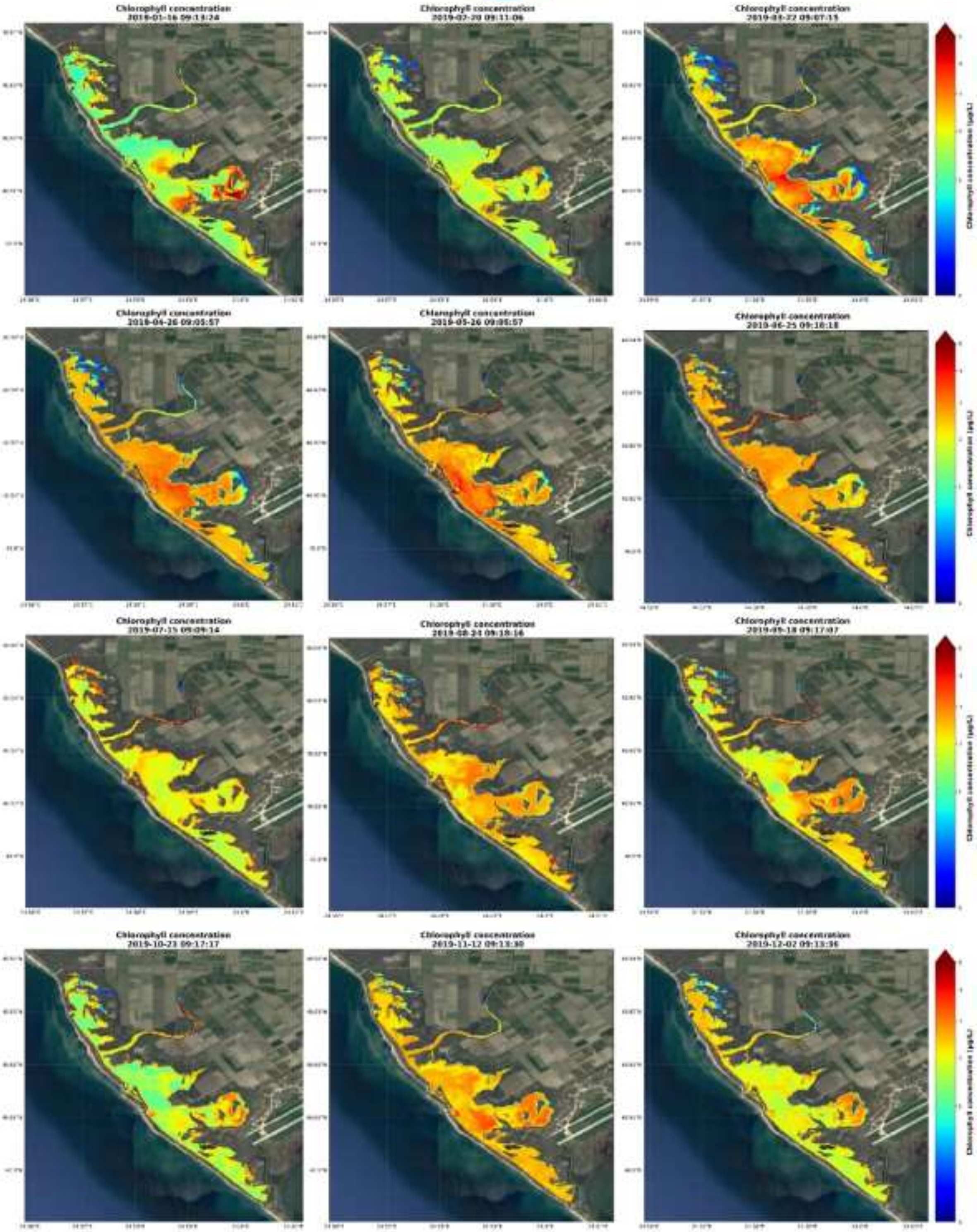

Figure 32. Seasonal evolution of Chl-a concentration in Eratino lagoon for the year 2019, based on Sentinel 2 satellite images.

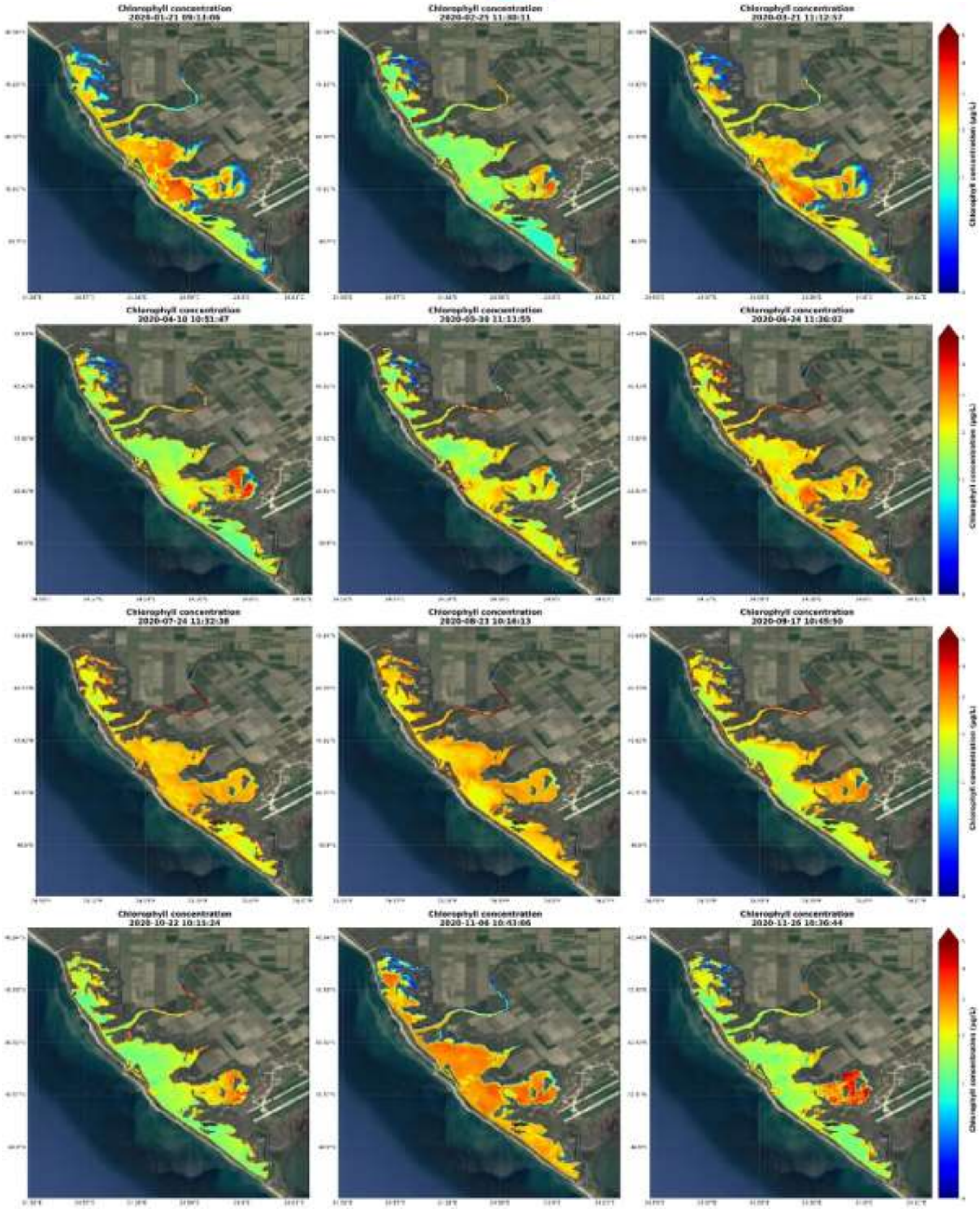

Figure 33. Seasonal evolution of Chl-a concentration in Eratino lagoon for the year 2020, based on Sentinel 2 satellite images.

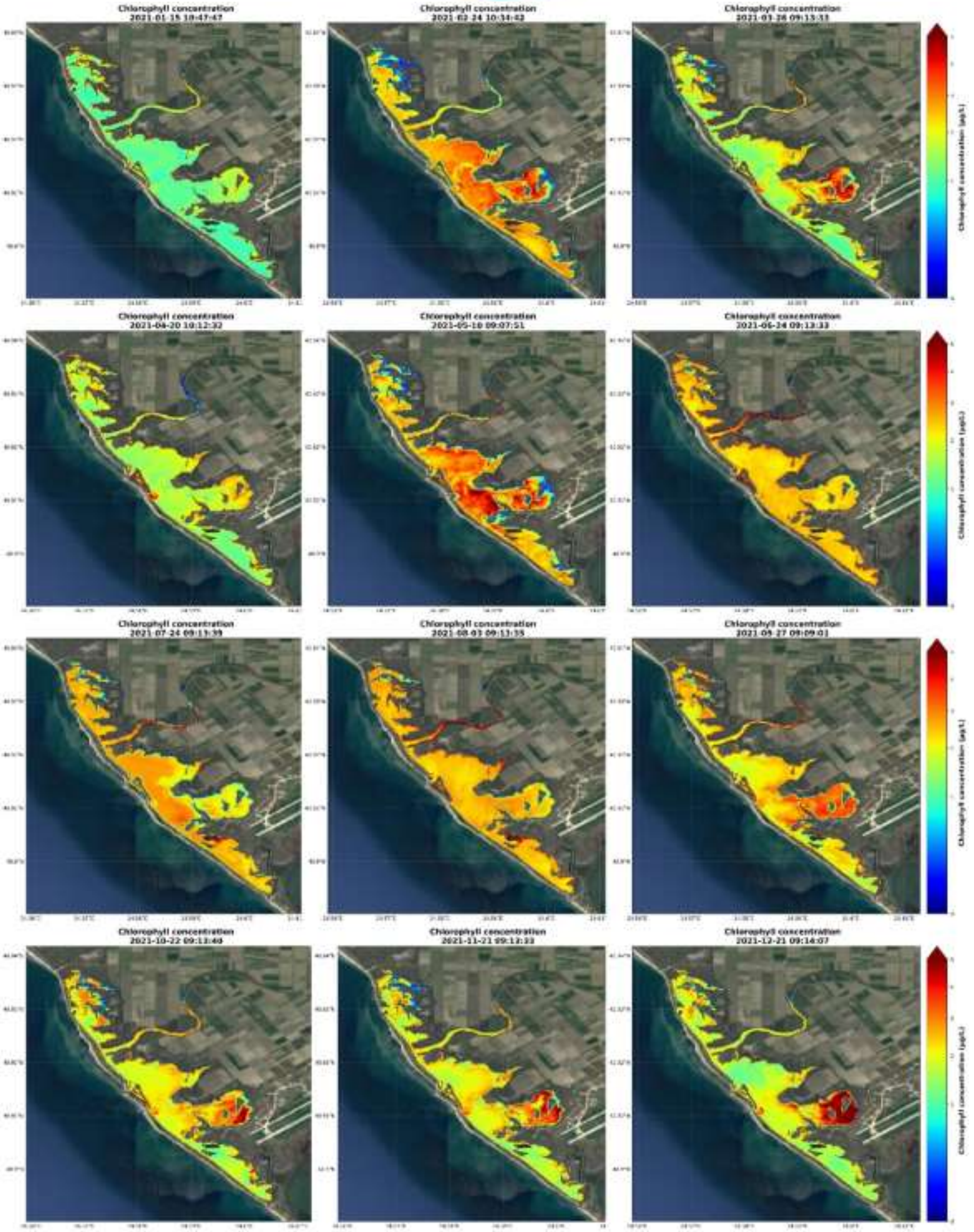

Figure 34. Seasonal evolution of Chl-a concentration in Eratino lagoon for the year 2021, based on Sentinel 2 satellite images.

3.1.3 Agiasma lagoon

Figures 32-41 show the spatial distribution of Chl-a in Agiasma lagoon for the years 2013-2021. In April 2013, high Chl-a values are determined at the western part of the lagoon (up to 45 μg/l), however low values are detected in the rest basin (around 1.5 μg/l). In July Chl-a increases, starting from the center of the lagoon. In the following months, Chl-a values decrease.

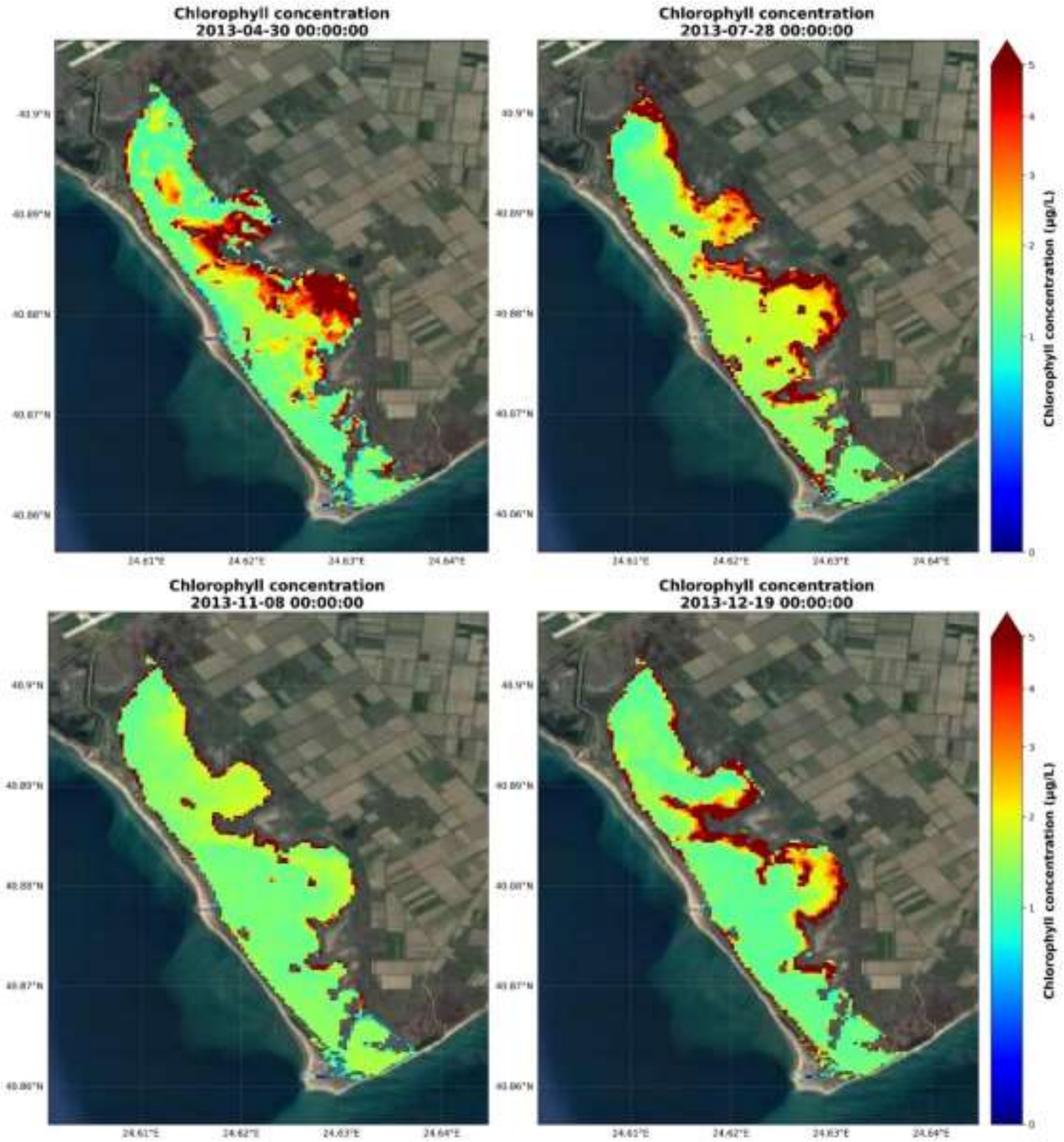

Figure 35. Seasonal evolution of Chl-a concentration in Agiasma lagoon for the year 2013, based on Landsat 8 satellite images.